POLITECNICO
MILANO 1863

SCUOLA DI INGEGNERIA INDUSTRIALE
E DELL'INFORMAZIONE

Risk Assessment of Uncontrolled Releases of Hydrogen and Methane Mixtures in Existing Methane Distribution Pipelines using CFD Simulations and Analytical Calculations

Tesi di Laurea Magistrale in
Chemical Engineering - Ingegneria Chimica

Author: **Andrea Atzori**

Student ID: 10752213
Advisor: Prof. Riccardo Mereu
Co-advisors: Marco Pontiggia
Academic Year: 2022-23

Abstract

In response to the accelerating concerns associated with climate change, this research investigates the potential of hydrogen as a sustainable energy vector, with an emphasis on using existing methane pipelines for hydrogen distribution. Recognizing the inherent risks of potential uncontrolled releases from pipelines carrying a hydrogen and methane mixture, a two-tiered strategy is introduced, involving the development of novel analytical models and the utilization of computational fluid dynamics (CFD) simulations. The focus lies in developing simulations to analyze the influence of physical obstructions on the expansion of the lower flammability limit cloud in mixed gas releases and in evaluating the qualitative characteristics of an eventual explosion. This data aims to improve safety measures, contributing to more efficient and environmentally conscious energy transition strategies.

Keywords: Sustainable energy, climate change, uncontrolled releases, CFD, hydrogen, natural gas, obstacle interaction

Abstract in lingua italiana

In risposta alle crescenti preoccupazioni associate ai cambiamenti climatici, questo lavoro di tesi esplora la capacità dell'idrogeno di agire come un vettore energetico sostenibile, con una particolare enfasi sull'utilizzo delle attuali condotte di metano per la distribuzione di idrogeno in miscela. Riconoscendo i rischi intrinseci delle possibili emissioni incontrollate da condotte che trasportano una miscela di idrogeno e metano, viene introdotta una strategia a due livelli, che coinvolge lo sviluppo di nuovi modelli analitici e l'utilizzo delle simulazioni di fluidodinamica computazionale (CFD). L'obiettivo è sviluppare delle simulazioni CFD in modo da analizzare l'influenza delle ostruzioni fisiche sull'espansione della nuvola con una concentrazione corrispondente al limite di infiammabilità inferiore e di valutare quantitativamente le caratteristiche di un'eventuale esplosione. Questi dati mirano a migliorare le misure di sicurezza, contribuendo a strategie di transizione energetica più efficienti e rispettose nei riguardi dell'ambiente.

Parole chiave: Energia sostenibile, cambiamento climatico, rilasci incontrollati, CFD, idrogeno, metano, interazioni con gli ostacoli

Contents

1 | Introduction

Considering the growing urgency of climate change, the critical role of hydrogen as a sustainable energy vector has come to the fore. The incorporation of hydrogen into the energy matrix promises substantial benefits for environmental sustainability, particularly due to its ability to produce zero-emission energy across a range of sectors. A novel approach towards decarbonization is proposed through the use of pre-existing methane pipelines for hydrogen distribution, facilitating a cost-effective and smoother transition from traditional fossil fuels.

However, the increased integration of methane pipelines carries a degree of risk, given the notable frequency of accidents within domestic methane distribution networks. Uncontrolled methane releases, with their potential for ignition and substantial harm, are further complicated by the presence of high-pressure jets and physical obstructions affecting the dispersion of the methane plume. Consequently, basic open-field modelling techniques fall short of capturing these complex dynamics, emphasizing the necessity for the consideration of real-world obstacles in these scenarios. In order to navigate these complexities, this research puts forth a two-pronged approach involving the creation of new analytical models and the use of computational fluid dynamics (CFD) simulations. These original analytical models, formulated specifically for this work, provide an idealistic representation of the various release scenarios in different conditions. Simultaneously, the advanced CFD software enables a precise simulation of the influence of realistic obstacles within potential release scenarios, including the structural complexities typical of distribution networks.

The primary objective of this research is to utilize the bespoke analytical models to theoretically describe the various release scenarios, and then employ CFD simulations to provide a realistic and analog perspective. By comparing these two approaches, we aim to better understand the impact of obstructions on the expansion of the lower flammability limit cloud and the potential implications of these releases. The central aim of this work is to leverage the power of CFD simulations to elucidate the impact of obstructions on the spread of the lower flammability limit cloud, and compare these insights with current

analytical models. In doing so, the research aims to clarify the possible implications of releases within these environments. The importance of CFD modelling thus takes center stage, providing critical data to develop safer, more efficient, and environmentally conscious energy transition strategies.

1.1. Concerning Hydrogen

Hydrogen, the first element in the periodic table, holds the distinction of being the lightest and most abundant element in the universe, constituting approximately 75% of mass or 90% of volume in all matter. On Earth, hydrogen is predominantly found in compounds with nearly every other element. While hydrogen can exist independently as a free element in the atmosphere, its presence is limited to less than 1 part per million by volume. Notably, ionic hydrogen, existing in a free state, exhibits greater reactivity compared to molecular hydrogen, which consists of two hydrogen atoms forming a nonpolar covalent compound. In 1776, Henry Cavendish identified hydrogen as a distinct species, and seven years later, Antoine Lavoisier coined the term "water maker" for hydrogen after demonstrating its composition in water alongside oxygen.

The most prevalent isotope of hydrogen is protium (H-1, H), possessing an atomic mass of 1.007822. The second isotope, deuterium (H-2, D), commonly referred to as heavy hydrogen, was discovered in 1932 by H. C. Urey and colleagues and is stable in nature. Deuterium exhibits slight variations in physical and chemical properties when compared to protium (H-1). Naturally occurring hydrogen contains approximately 0.014% deuterium. Deuterium primarily combines with hydrogen atoms to form the diatomic compound HD, with a fraction of approximately 0.032% in natural hydrogen. The presence of molecular deuterium is highly unlikely. The third isotope of hydrogen is tritium (H-3, T), which is radioactive and has a half-life of 12.3 years. Tritium was discovered by E. Rutherford in 1934. Furthermore, isotopes such as H-4, H-5, and H-7, which have short lifespans, have been synthesized subsequently.

1.1.1. Physical properties of Hydrogen

Hydrogen, functioning as an ideal gas, demonstrates favorable properties across a broad temperature range and even at high pressures. Under standard temperature and pressure conditions, it manifests as a colorless, odorless, tasteless, non-toxic, non-corrosive, and non-metallic diatomic gas, which is generally considered physiologically safe. Its notable characteristic is its low density, necessitating compression or liquefaction for practical applications. Notably, hydrogen displays positive buoyancy above 22 K, encompassing

the majority of its gaseous state temperature range [22].

Hydrogen gas exhibits high diffusion capability and buoyancy, swiftly intermixing with the surrounding air upon release. The rate of diffusion is proportionate to the diffusion coefficient and varies with temperature according to T^n, where the exponent n ranges between 1.72 and 1.8. Consequently, hydrogen diffusion rates in air are approximately four times higher compared to the diffusion rates of air itself. The upward velocity driven by positive buoyancy is not directly determinable, as it depends on the density disparity between hydrogen and air, as well as drag and friction forces, volume size and shape, and atmospheric turbulence. While the positive buoyancy of hydrogen is advantageous in unconfined areas, it can pose risks in partially confined spaces where hydrogen can accumulate, such as beneath a roof. Both diffusion and buoyancy govern the rate at which hydrogen mixes with ambient air. Rapid mixing with air raises safety concerns, as it quickly leads to flammable mixtures that, conversely, dilute rapidly to non-flammable levels. Therefore, it is estimated that only a fraction of the gas mixture cloud is involved in a typical unconfined hydrogen explosion, releasing a few percent of the theoretically available energy.

Due to its small size, low molecular weight, and low viscosity, hydrogen presents challenges regarding its propensity to leak at a higher molecular flow rate compared to other gases. Even minimal amounts of diffusion can occur through intact materials, particularly organic substances, resulting in gas accumulation in confined spaces. Leakage rates are approximately 50 times higher than for water and 10 times higher than nitrogen. While the addition of odorants or colorants could aid in detecting small leaks, this practice is often impractical and not feasible for liquid hydrogen (LH2).

Hydrogen gas dissolved in liquids permeates into adjacent vessel materials. At elevated temperatures and pressures, hydrogen severely affects mild steels, causing decarburization and embrittlement. This poses a significant concern in any scenario involving the storage or transfer of pressurized hydrogen gas. Appropriate material selection, such as special alloy steels, and technology are necessary to prevent embrittlement.

Hydrogen exists in two forms, ortho and para hydrogen, with their distribution dependent on temperature. At room temperature, normal hydrogen consists of approximately 75% ortho (aligned nuclear spins) and 25% para (anti-aligned spins). In the lower temperature range (< 80 K), para hydrogen becomes the more stable form. At 20 K, the thermal equilibrium concentrations are 99.821% para and 0.179% ortho, with the transition requiring several days to establish a new equilibrium state. However, magnetic impurities and even small oxygen concentrations can catalyze ortho-para conversions, accelerating the process

by several orders of magnitude (e.g., Fe(OH)3) to hours. Catalysts can generate any concentration of either spin state at any temperature. The two spin states exhibit minimal differences in most physical properties, with the primary distinction lying in their significant energy difference, resulting in notable discrepancies in specific heats and thermal conductivities. The presence of a radiation field generates free hydrogen atoms and ions, acting as catalysts before recombining and producing excess ortho hydrogen.

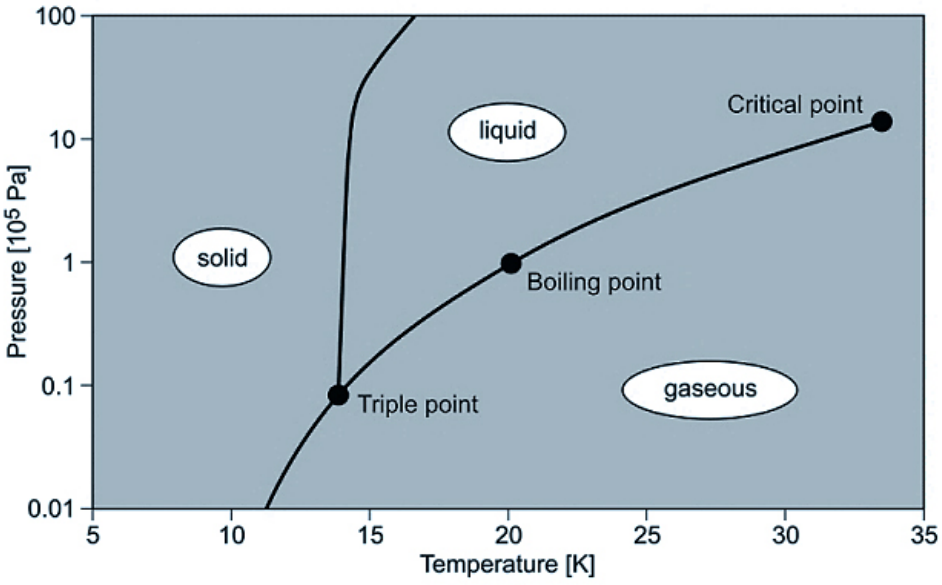

Figure 1.1: Phase diagram of hydrogen.

Additionally, hydrogen demonstrates a positive Thompson-Joule effect above the inversion temperature of 193 K. This means that the temperature of hydrogen gas increases upon depressurization, which can potentially lead to ignition. For instance, a six-degree temperature change occurs during a sudden pressure drop from 20 MPa to ambient pressure. However, the likelihood of spontaneous ignition solely due to this effect is low; instead, an explosion is more probable due to electrostatic charging of dust particles during depressurization or autoignition at high temperatures.

1.1.2. Chemical properties of Hydrogen

Hydrogen readily undergoes chemical reactions with both non-metals, characterized by high electronegativity, and metals, characterized by low electronegativity, resulting in the formation of ionic or covalent hydrides (e.g., HCl, H2O). The electronegativity of hydrogen, measured on the Pauling scale, is 2.20. Hydrogen exhibits high flammability when combined with oxygen across a broad range of concentrations. As a fuel, it represents

a clean and environmentally benign energy source. The mass-specific energy density of hydrogen is remarkably high, with 1 kg of hydrogen containing approximately 132.5 MJ, which is approximately 2.5 times the energy content of 1 kg of natural gas. The energy content of hydrogen is quantified as either the lower heating value (LHV) of 242 kJ/mol or the higher heating value (HHV) of 286 kJ/mol. The substantial difference of 15.6%, compared to other gases, stems from the heat released upon condensation of water vapor, which can be harnessed in a turbine but not in a fuel cell. A stoichiometric hydrogen-air mixture, where all the fuel is consumed during the reaction, resulting in the release of maximum combustion energy, comprises 29.5 vol% of hydrogen. The combustion product of hydrogen is water vapor. When burning, it produces a non-luminous, nearly invisible pale blue flame, generating water vapor while liberating chemically bound energy as heat (gross heat of combustion). The flame temperature of a burning premixed stoichiometric hydrogen-air mixture reaches a maximum of 2403 K. Hydrogen exhibits a wide flammability range (at room temperature) spanning from 4 to 75 vol% concentration in air, and up to 95 vol% in oxygen. The lower flammability limit (LFL), which represents the minimum amount of fuel capable of sustaining combustion, is typically considered the more critical limit since it is reached first in cases of continuous leakage. The flammability range expands as the temperature increases. The influence of temperature is expressed in the modified Burgess-Wheeler equation for the LFL of hydrogen at ambient pressure as it is shown in equation (1.1), where ΔHc represents the net heat of combustion, and T is given in Kelvin [27].

$$C_{LFL} = C_{LFL}(300K) - \frac{3.14}{\Delta H_c}(T - 300) = 4.0 - 0.013(T - 300)\ [vol\%] \tag{1.1}$$

Besides, the corresponding equation for the upper flammability limit (UFL) is given by the modified Burgess-Wheeler equation for the LFL of hydrogen at ambient pressure [12] as it is shown in equation (1.2).

$$C_{UFL} = 74.0 - 0.026(T - 300)\ [vol\%] \tag{1.2}$$

The danger of a hydrogen-air mixture explosion is significant due to its low ignition energy, fast burning velocity, and the potential for detonation. Hydrogen has a high auto-ignition temperature (800-1000 K), but this can be reduced by catalytic surfaces. Hydrogen lacks a flash point since it's a gas at room temperature, implying cryogenic hydrogen will flash at any temperature above its 20 K boiling point.

The energy required to ignite hydrogen concentration in air, or minimum ignition energy,

is a meagre 0.02 mJ, significantly lower than other hydrocarbon-air mixtures. This energy decreases as temperature, pressure, or oxygen content increase. Hydrogen's hot air jet ignition temperature is the lowest among all hydrocarbons and it depends on jet diameter, velocity, and mixture composition.

Hydrogen's "maximum experimental safe gap" (MESG) is 0.08 mm, denoting the greatest distance that permits flame propagation between two plates. The "quenching gap", the distance at which a flammable mixture's ignition is suppressed, is 0.64 mm for hydrogen. Given the intense explosion pressures, the MESG is invariably less than the quenching gap.

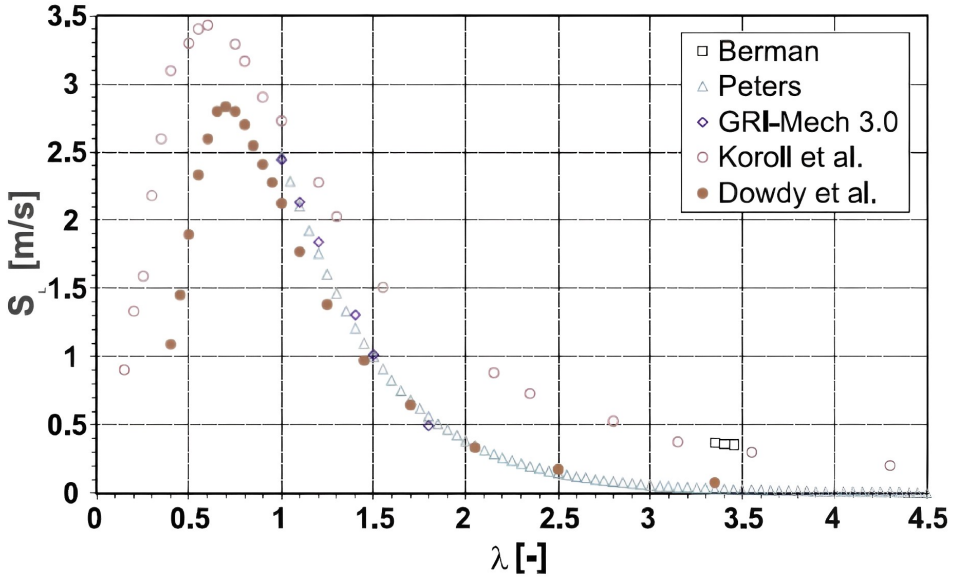

Figure 1.2: Burning velocities in hydrogen-air mixtures as measured by various authors.

Hydrogen's burning velocity, indicating a combustion wave's advancement speed into a static flammable mixture, is 2.55 m/s under stoichiometric ambient conditions, rising to 3.2 m/s at a concentration of 40.1%. It's superior to other hydrocarbon fuel-air mixtures due to hydrogen's swift chemical kinetics and high diffusivity. An elevated burning velocity heightens the possibility for deflagration to detonation transition (DDT). In contrast, flame speed greatly exceeds burning velocity as it accounts for the expansion of combustion products, instabilities, and flame deformation. A deflagrative burning flame's top speed, defined by the speed of sound in the gas mixture, is 975 m/s for a stoichiometric hydrogen-air mix.

The detonability range, typically stated as 18-59 vol% of hydrogen concentration, can vary based on the system size. For instance, in Tieszen et al. [40] a range of 13-70% of H2

for a 43 cm tube was noted, and the Russian RUT facility observed a lower limit as low as 12.5 vol%. Pure oxygen extends the detonation range to 15-90% [27], with detonation velocity reaching 2000 m/s in air and 3500 m/s in pure oxygen.

Detonation cell size, a reactivity measure, can indicate DDT, with smaller cells implying higher reactivity. A hydrogen-air stoichiometric mix with a cell size of 15 mm is quite reactive. As mixtures deviate from stoichiometry, cell sizes increase. An empirical law correlating cell size and critical tube diameter has allowed the development of a surface energy model to derive a critical initiation charge weight for various mixtures.

The critical tube diameter, representing the smallest diameter needed for a detonation wave to transition from a tube to an unconfined cloud, and the detonation initiation energy, or minimum energy needed to initiate a detonation wave, are other critical measures. For hydrogen-air stoichiometric mix to detonate, a tube length over diameter ratio of around 100 is typical.

Experience shows that an accidental hydrogen release from a failed storage tank or pipeline results in an explosion liberating only 0.1-10%, usually less than 1%, of its thermal energy [5]. An explosion of a hydrogen-air mixture cloud forms a pressure wave, with its overpressure effects to be discussed later in this paper.

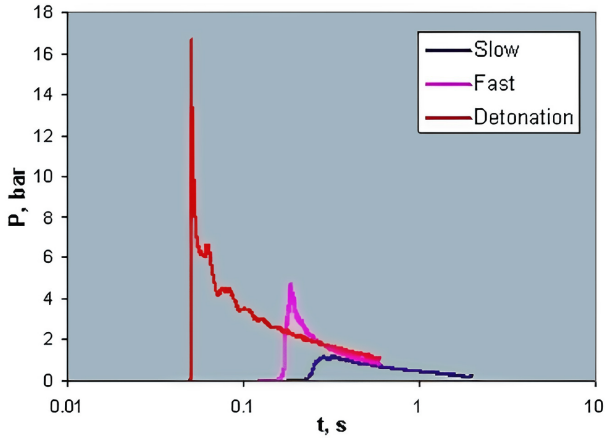

Figure 1.3: Pressure signals considering different hydrogen combustion modes.

A flame's radiated thermal energy corresponds to its higher heating value, which can be lowered by atmospheric moisture absorption. The radiation from a hydrogen flame is relatively low due to ambient water vapour absorption, meaning despite its high flame temperature, the burning hazard is minimal. The flame's low visibility makes it hard to detect and localize, though a benefit is the absence of smoke in hydrogen-air fires, critical for confined areas [16].

1.1.3. Hazards

Hydrogen hazards can manifest in different forms such as physiological, including asphyxiation, thermal burns, frostbite, hypothermia, and overpressure injury, physical, including component failures due to low temperature effects and hydrogen embrittlement, and chemical, such as combustion or explosion [33][34]. The primary concern is accidentally creating a flammable or explosive mixture with air.

While we have accumulated considerable knowledge regarding the flammability and detonation limits of various hydrogen mixtures and the impact of different variables, such as ignition sources, autoignition temperature, and quenching gap, there is still much work to be done on other aspects. These include understanding the deflagration-to-detonation transition (DDT), the compatibility of hydrogen with different storage materials, and its behavior under extreme storage and use conditions. The 2011 explosion at the Fukushima Daiichi nuclear power complex in Japan has dramatically highlighted the gaps in our knowledge and underscored the need to learn from past accidents [32].

Achieving safety in the use of hydrogen requires that both designers and operational personnel be fully aware of the range of hazards associated with handling and using this substance. Most of the hazards with hydrogen stem from its innate properties as an odorless, colorless, and tasteless gas, making leaks hard to detect without technological assistance. Therefore, hydrogen sensors are a common tool in the industry to detect such leaks. By comparison, natural gas, which shares these properties, often has odorants added to make it perceptible to people. However, this strategy is not feasible with hydrogen as all known odorants contaminate fuel cells, a popular application for hydrogen, and are also unacceptable in food applications such as the hydrogenation of edible oils [33].

Another example could be the recent accident that occurred in the Gangwon province in Korea in May 2019. As a matter of fact, a catastrophic hydrogen tank explosion took place, resulting in the tragic loss of two lives and causing extensive damage to several structures, some of which were located more than 100 meters away from the explosion site. Investigations into the incident revealed that the cause of the explosion was the infiltration of oxygen into the hydrogen storage tank [17]. The explosion accident led to significant concerns about the safety of hydrogen energy, particularly in the context of Hydrogen Refueling Stations (HRSs) that were being built in cities. Potential risks associated with hydrogen energy have been highlighted after this particular episode, including the possibility of explosion accidents, which could lead to blast waves and debris scattering [18]. This incident serves as a sharp reminder of the potential hazards and destructive consequences associated with hydrogen handling and the related explosion hazard. The

public's fear and apprehension, triggered by such events, can pose significant challenges to the advancement of sustainable strategies. Therefore, it is imperative to achieve a high standard of safety in hydrogen utilization to encourage public confidence and facilitate the broader adoption of this energy source.

2 | Theoretical Background

2.1. Jets in literature

When considering the scenario of gas discharge directed towards large obstacles in close proximity, the expectation is the formation of an impinged jet. Characteristically, high momentum jets in open fields exhibit high velocities relative to the ambient air, resulting in significant air entrainment. However, upon impact with a nearby obstacle, a sudden decrease in gas velocity is observed. This reduction diminishes air entrainment and generally extends the range of potential damage, as corroborated by previous studies [28].

Under-expanded jets have been extensively researched throughout history, leading to a comprehensive understanding of their structure [11]. This knowledge is crucial due to the wide range of practical engineering applications and situations where these jets are involved, such as aircraft exhaust, rocket propulsion [37], parallel injection and supersonic combustors [42], and various industrial releases, including discharge from rupture disks or accidental leakage of pressurized fluids [29].

In recent years, the focus has shifted towards the study of impinging jets for industrial safety. Numerous attempts have been made to investigate the behavior of jets in relation to obstacles positioned near or directly in front of the outflowing surface. These studies have been conducted both numerically and experimentally, examining the effects of various obstacles such as cylindrical objects [39], surfaces [2, 13, 15], vertical surfaces [1], spheres [8], large obstacles, barrier walls [6, 36], and cylinders [24].

Despite the wealth of research, there is a noticeable gap in the current state of the art. Specifically, there is a lack of adequate models to handle jets in structures that closely resemble real-world scenarios, such as gas reduction cabins. Furthermore, no practical tools for risk assessment have been provided in the existing similar studies. This highlights the significance of obstacles in risk evaluation and the need for further research in this area, particularly in developing models that can accurately represent real-world structures.

A free jet is characterized as a jet whose dynamics are not affected by its surroundings,

meaning it does not interact with the ground, walls, or any form of obstacle. As reported [6] for subsonic jet and by [4] for supersonic ones, The concentration profile within the jet undergoes variations in relation to the axial position, denoted as x, and the radial position, denoted as r. The fluctuations in the concentration profile can be ascribed to the impacts of turbulence and entrainment effects. The reduction in the mean mole fraction of the discharged substance X, in relation to the axial coordinate, can be articulated through the following expression:

$$\bar{\eta} = \frac{KD}{x+a}\sqrt{\left(\frac{\rho_{air}}{\rho_{gas}}\right)} \tag{2.1}$$

in equation 2.1:

- D represents the diameter of the orifice. In the context of a subsonic release, it refers to the actual diameter, whereas in the case of a supersonic jet, it denotes the equivalent diameter;
- K signifies the decay constant. For a supersonic jet, this constant is expected to be within the range of 4 to 5.5 [4];
- a represents the displacement from the original source;
- ρ_{air} is the air density;
- ρ_{gas} is the gas density at the ambient condition (pressure and temperature);
- x is the jet axial coordinate [24];

As reported by [35], the radial profile can be calculated using a Gaussian profile, which can be expressed as follows:

$$C(s,r,\theta) = C0(s)\exp\left(-\frac{r^2}{S_c^2 b^2(s)}\right) \tag{2.2}$$

in equation 2.2:

- S_c corresponds to the Schmidt Number;
- r corresponds to the jet radial coordinate;
- s is a coordinate that identify the position along the jet axis centreline;
- b is the local lateral dimension of the jet, that depend on s, goes from 0 to r;
- θ is the angle between the ground and the local ;

- $C0$ is the concentration at the release point;
- C is the actual concentration in dependence of s, r, θ;

2.1.1. Jet's Structure

The occurrence of an under-expanded supercritical jet is typically observed when the fluid pressure at the orifice, whether it be a nozzle or an accidental opening, exceeds twice the ambient pressure. Historically, the transient behavior of the jet has not been the subject of extensive study. In contrast, the steady-state flow conditions have been thoroughly investigated, primarily due to their frequent occurrence. The defining characteristics of a jet include compressible and viscous effects, which collectively determine its overall structure [47]. As depicted in Figure 2.1.1, it is common to categorize the development of the jet into three distinct zones:

- Nearfield zone.
- Transition zone.
- Farfield zone.

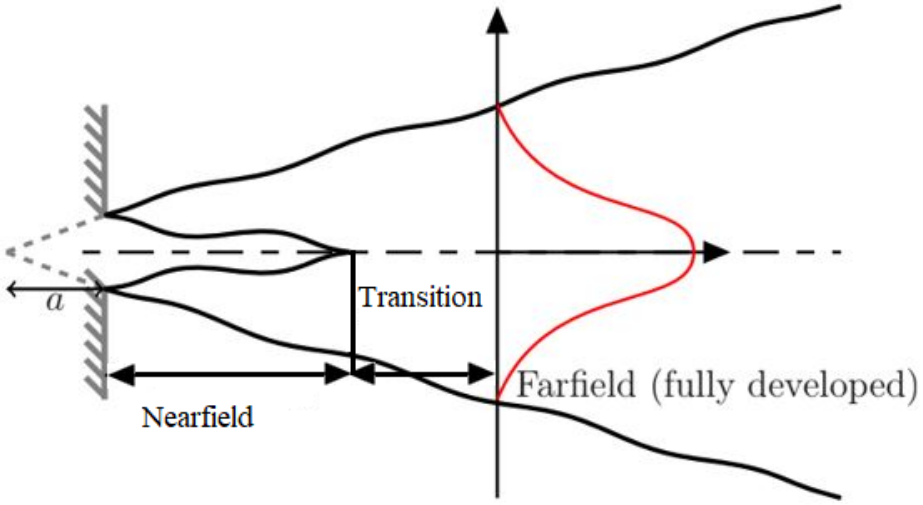

Figure 2.1: Jet Zones Subdivision.

The Nearfield zone is divided into two distinct sections: the core region and the region known as the mixing layer [47]. In the first section, the flow is isolated from the ambient fluid and its behavior is predominantly governed by compressible effects. This characteristic is the reason why this zone is often referred to as the gas dynamic region. Thus, the fluid experiences an iso-entropic expansion, followed by a recompression through shock

waves [24].

Within the mixing layer, turbulence effects facilitate an exchange between the ejected and ambient fluids. This exchange is marked by the presence of large turbulent structures, or eddies, which progressively expand downstream of the flow. The termination of the nearfield zone is signified when the sonic line reaches the axis, as illustrated in Figure 2.1. Consequently, the mixing layer fully supersedes the inner part. This point marks the commencement of the Transition zone, where the variation of the variables is constrained, both longitudinally and radially. This constraint promotes enhanced mixing of the outflowing and surrounding fluids, leading to a homogenization of the pressure field. From this point forward, entrainment occurs everywhere.

In the Fairfield zone, the jet is fully expanded and the flow is developed, with its mean characteristics such as pressure, temperature, and velocity reaching a state referred to as similarity [11, 21]. From a qualitative perspective, similarity implies that the normalized radial profiles of the mean variables adhere to the same law and can be represented by a Gaussian profile. The characteristics on the axis of the jet are inversely proportional to the distance from the inlet Section.

2.2. Models Classification

The dynamics of a release into the atmosphere can be categorized into three distinct downstream regions:

- Inertial Phase.
- Buoyancy Phase.
- Dispersion Phase.

In the initial region, known as the Inertial Phase, inertial forces are predominant and the jet maintains a well-defined shape. As the velocity decreases to a certain threshold, the second region, the Buoyancy Phase, becomes discernible. In this phase, buoyancy forces are the driving phenomenon, and depending on the gas density, a distinct behavior can be observed in comparison to air density. Ultimately, when the velocity reduces sufficiently, the Dispersion Phase commences. This phase is characterized by the dominance of atmospheric turbulent mixing phenomena and significant air entrainment, resulting in an expansion of the jet dimensions.

Essentially, the mathematical instruments that can be utilized to model the behavior of a jet can be categorized into three distinct classifications [14]:

- Gaussian Models.
- Integral Models (Tube Flow).
- CFD Models.

Gaussian Models are the most straightforward models [25]. They are based on simplified mathematical models and semi-empirical equations. These methods are capable of predicting only the final region of a release, specifically the farfield zone. A key advantage of these methods is the low level of user expertise required to solve the equations.

Integral Models, while requiring a reasonable computational cost, offer a more precise prediction compared to Gaussian models. These models are often lumped-parameters models. However, their limitation lies in their inability to accommodate complex geometries and obstacles, making them applicable only under open field conditions. Furthermore, the calibration of the constant parameter used by these models has been validated through experimental comparison, which means that they are reliable only for the scenarios they have been validated against.

CFD models implement the Navier-Stokes, mass conservation, species transport, and energy equations, in conjunction with suitable turbulence models and boundary conditions. This category of models is the most accurate, capable of realistically representing all three regions of a release. The primary disadvantages are the substantial computational resources required and the high level of user expertise needed.

2.3. CFD modelling for Safety Applications

For what concerns safety analysis and risk evaluation, Computational Fluid Dynamics (CFD) modelling has been a frequently employed tool in the past [7, 28]. This can be attributed to the significant advancements made in the computer industry in recent years, which have rendered CFD a viable instrument for investigating complex problems [19].

When it comes to safety-related issues, only a limited number of similar studies have been conducted in recent years, primarily focusing on high-pressure methane jets. A notable contribution to this field has been made by [3], who concentrated their research efforts on the behavior of both methane and hydrogen jets. Their work specifically examined the impact of the ground on the maximum extension of the Lower Flammable Limit (LFL) zone.

Following a similar trajectory, an analysis has been conducted on the interaction between methane jets and the ground, exploring different models for the Equivalent Diameter [30]. This research contributes to a deeper understanding of the dynamics between methane jets and their environment.

Furthermore, CFD has been utilized to investigate the impingement phenomena of high-pressure jets on large obstacles. Their findings were then compared with the results derived from the integral model, providing a comprehensive perspective on the behavior of high-pressure jets when interacting with substantial obstacles. This comparative approach enhances the depth and breadth of knowledge in this field, paving the way for future research and development [28].

3 | Materials and Methods

3.1. Computational Fluid Dynamics

Computational Fluid Dynamics (CFD) stands as a groundbreaking method in fluid dynamics analysis. It offers an intricate, detailed approach to analyzing and predicting fluid behavior, solidifying its position as an invaluable tool in the field of engineering and applied sciences. At the heart of CFD is a process predicated on the numerical solution of transport equations, executed over a computational grid referred to as a 'mesh.' This technique utilizes mathematical models to simulate and analyze the interaction between flows and their boundaries, thereby enabling a thorough investigation of complex fluid dynamics problems.

In an increasingly digital world, where precision, accuracy, and efficiency are paramount, numerous general-purpose codes for CFD simulations have been developed. These codes cater to a broad spectrum of applications and tasks, ranging from basic flow analysis to intricate simulations involving turbulence, heat transfer, and chemical reactions. They serve as the cornerstone for various industrial and research activities, with their versatility and power driving the advancement of knowledge and technology in numerous fields.

Among the array of available software, the ANSYS® Fluent 2022 software has been predominantly employed in this work for conducting CFD simulations. Fluent, an integral part of the comprehensive ANSYS® suite, is renowned for its robust capabilities and sophisticated features. Rooted in a finite volume solver, Fluent implements the integral formulation of the conservation laws in a discretized manner directly within the physical space. The finite volume method is a highly efficient and accurate approach to solving partial differential equations that represent the conservation laws of fluid dynamics.

This numerical methodology is based on the local conservation principle, which posits that the amount of a conserved quantity entering a control volume minus the amount leaving the control volume must equal the rate of change of the quantity within the volume. By applying this principle to many control volumes that collectively cover the computational domain, Fluent can solve complex fluid dynamics problems.

The finite volume method employed by Fluent offers the advantage of compatibility with arbitrary meshes. In other words, Fluent can operate with a wide variety of mesh types, including structured, unstructured, or hybrid grids, and shapes such as tetrahedral, hexahedral, or polyhedral cells. This flexibility allows the user to optimize the mesh to the specific requirements of each simulation, ensuring the highest level of accuracy while maintaining computational efficiency.

The control volumes, the fundamental building blocks of the computational grid, can be defined in myriad ways within Fluent, offering a significant degree of freedom and customization. The choice of control volume impacts the discretization of the conservation laws and consequently influences the accuracy and convergence of the solution. This flexibility in defining control volumes empowers users to tailor the simulation to the unique requirements of each fluid dynamics problem, ensuring the highest fidelity in capturing the behavior of the flow.

In conclusion, the Computational Fluid Dynamics technique, with its potent numerical solutions and mesh-based methodology, provides a comprehensive approach to fluid dynamics analysis. The application of the ANSYStextsuperscript® Fluent 2022 software, with its finite volume solver and flexible mesh capabilities, amplifies the power and precision of this technique. As we delve deeper into the intricacies of CFD simulations, it is essential to recognize the foundational role played by such robust software tools, which serve as the catalyst in our quest to understand and master the complexities of fluid dynamics.

3.1.1. Conservation law in general form

A scalar quantity per unit volume U, existing in an certain fixed volume, fixed in space, is taken into account, enclosed by a distinct closed surface S. The local intensity of U varies through the effect of fluxes $\vec{F}$, which express the contributions from the surrounding points to the local value, and through sources Q. The general form of a conservation law is expressed stating that the variation per unit time of the quantity U within the volume Ω should be equal to the net contribution from the incoming fluxes through the surface S, plus contributions from the sources of the quantity U, divided into volume and surface sources, Q_V and $\vec{Q_S}$. Hence, the general form of the conservation equation for the quantity U is:

$$\frac{\partial}{\partial t}\int_{\Omega} U d\Omega + \oint_S \vec{F}\cdot d\vec{S} = \int_{\Omega} Q_V d\Omega + \oint_S \vec{Q_S}\cdot d\vec{S} \tag{3.1}$$

If the Gauss's theorem for continuous fluxes and surfaces sources is being applied, it is possible to obtain the following differential form:

$$\frac{\partial U}{\partial t} + \vec{\nabla} \cdot \vec{F} = Q_V + \vec{\nabla} \cdot \vec{Q_S} \tag{3.2}$$

The flux vector has two main components: the convective flux $\vec{F_C}$, which is the amount of U transported with the motion $\vec{F_C} = vU$, and diffusive flux F_D, the contribution present in fluids at rest due to the molecular, thermal agitation. The latter can be articulated through the application of Fick's generalized gradient law: $\vec{F_D} = -\kappa\rho\vec{\nabla}u$, with v as the velocity vector, u as U per unit of mass, ρ as the fluid density, and κ as a diffusivity constant. The earlier stated equation then becomes:

$$\frac{\partial \rho u}{\partial t} + \vec{\nabla} \cdot (\rho \vec{v} u) = \vec{\nabla} \cdot \left(\kappa\rho\vec{\nabla}u\right) + Q_V + \vec{\nabla} \cdot \vec{Q_S} \tag{3.3}$$

Considering the conserved property being described by a vector quantity $\vec{U}$, then the flux becomes a tensor $\overline{F}$, the volume source term a vector $\vec{Q_V}$, and therefore the equation 2.1 becomes:

$$\frac{\partial}{\partial t}\int_\Omega \vec{U} d\Omega + \oint_S \overline{F} \cdot d\vec{S} = \int_\Omega \vec{Q_V} d\Omega + \oint_S \overline{Q_S} \cdot d\vec{S} \tag{3.4}$$

That can also be written in the following alternative differential form:

$$\frac{\partial \vec{U}}{\partial t} + \vec{\nabla} \cdot \left(\overline{F} - \overline{Q_S}\right) = \vec{Q_V} \tag{3.5}$$

3.1.2. The mass conservation equation

The conservation of mass law is a universal statement of a kinematic principle, which remains unaffected by the characteristics of the fluid, or the external forces applied to it. This law conveys an experimentally observed phenomenon stating that within a fluidic system, mass cannot be spontaneously lost or generated. Notably, no diffusion flux or source term is associated with mass transportation. Under these circumstances, the conservation equation becomes:

$$\frac{\partial}{\partial t}\int_{\Omega}\rho d\Omega + \oint_{S}\rho\vec{v}\cdot d\vec{S} = 0 \tag{3.6}$$

Utilizing Gauss's theorem, the surface integral, which is used for the convective flux, can be transformed into a volume integral, subsequently leading to the derivation of its differential form:

$$\frac{\partial\rho}{\partial t} + \vec{\nabla}\cdot(\rho\vec{v}) = 0 \tag{3.7}$$

3.1.3. The momentum conservation law

According to Newton's laws, the changes in momentum within a physical system are attributed to the forces exerted on it. These forces include the external volume forces, denoted as $\vec{f}_e$, and the internal forces, denoted as $\vec{f}_i$. The internal forces are contingent on the specific characteristics of the fluid in question and are derived from the assumptions made regarding the properties of the internal deformations within the fluid and their correlation with the internal stresses. When the fluid is assumed to be Newtonian, the total internal stresses, represented as $\overline{\sigma}$, are defined as follows:

$$\overline{\sigma} = -p\overline{I} + \overline{\tau} \tag{3.8}$$

Where $\overline{I}$ represents the unit tensor. The equation introduces the presence of the isotropic pressure component, denoted as $p\overline{I}$. Additionally, $\overline{\tau}$ is the viscous shear stress tensor, which is defined as per Stokes' equation

$$\tau_{ij} = \mu\left[(\partial_i v_j + \partial_j v_i) - \frac{2}{3}\left(\vec{\nabla}\cdot\vec{v}\right)\delta_{ij}\right] \tag{3.9}$$

Where μ denotes the dynamic viscosity of the fluid. As with the mass conservation equations, the assumption is made that momentum diffusion is not feasible in a stationary fluid, thereby eliminating any diffusive contribution. The source term is composed of the sum of the external volume forces per unit volume, represented as $\rho\vec{f}_e$, and the aggregate of all internal forces. By definition, integral forces within every point inside the volume cancel out in pairs. Consequently, the residual internal forces within the volume Ω are those exerted on the points of the boundary surface, as they lack an opposing counterpart

within the considered volume. As such, the internal forces function as surface sources, with an intensity represented by $\int_S \overline{\sigma} \cdot d\vec{S}$. This leads to the following form of the momentum conservation equation:

$$\frac{\partial}{\partial t}\int_\Omega \rho\vec{v}d\Omega + \oint_S \rho\vec{v}\left(\vec{v}\cdot d\vec{S}\right) = \int_\Omega \rho\vec{f}_e d\Omega - \oint_S p d\vec{S} + \oint_S \overline{\tau}\cdot d\vec{S} \tag{3.10}$$

Applying Gauss's theorem, the differential form of the equation of motion, known as the Navier-Stokes equations, can be derived:

$$\frac{\partial}{\partial t}\left(\rho\vec{v}\right) + \vec{\nabla}\cdot\left(\rho\vec{v}\otimes\vec{v} + p\overline{I} - \overline{\tau}\right) = \rho\vec{f}_e \tag{3.11}$$

3.1.4. The energy conservation equation

According to the first law of thermodynamics, the changes in the total energy within a fluid are driven by the work performed by the forces acting on the system and the heat transferred to the system. When considering the general form of the conservation law for total energy, the convective energy flux, denoted as $\vec{F_C}$, should be expressed as follows:

$$\vec{F_C} = \rho\vec{v}\left(e + \frac{\vec{v}^2}{2}\right) = \rho\vec{v}E \tag{3.12}$$

The total energy per unit mass is denoted by E, while e is the internal energy per unit mass is. The diffusive flux, FD, is expressed as:

$$\vec{F_D} = -\gamma\rho\kappa\vec{\nabla}e \tag{3.13}$$

Here, the coefficient κ stands for the thermal diffusivity coefficient, which, along with the dynamic viscosity μ, needs to be empirically defined. The coefficient γ signifies the ratio of specific heat coefficients under constant pressure and constant volume. The diffusive flux, $\vec{F_D}$, can also be expressed in accordance with Fourier's law of heat conduction:

$$\vec{F_D} = -\xi\nabla\ \vec{T} \tag{3.14}$$

In this equation, T represents the absolute temperature and ξ is the thermal conductivity

coefficient. The volume sources comprise the sum of the work of the volume forces $\vec{f_e}$ and the heat sources other than conduction (such as radiation and chemical reactions), denoted by q_H.

$$Q_V = \rho \vec{f_e} \cdot \vec{v} + q_H \tag{3.15}$$

The surface sources, $\vec{Q_S}$, result from the work performed on the fluid by internal shear stresses acting on the surface of the volume, considering that there are no surface heat sources:

$$\vec{Q_S} = \overline{\sigma} \cdot \vec{v} = -p\vec{v} + \overline{\tau} \cdot \vec{v} \tag{3.16}$$

By integrating all these contributions, the energy equation in integral form is:

$$\frac{\partial}{\partial t} \int_\Omega \rho E d\Omega + \oint_S \rho E \vec{v} \cdot d\vec{S} = \oint_S \xi \vec{\nabla} T \cdot d\vec{S} + \int_\Omega \left(\rho \vec{f_e} \cdot \vec{v} + q_H \right) d\Omega + \oint_S (\overline{\sigma} \cdot \vec{v}) \cdot d\vec{S} \tag{3.17}$$

The equivalent differential form is:

$$\frac{\partial}{\partial t} (\rho E) + \vec{\nabla} \cdot (\rho E \vec{v}) = \vec{\nabla} \cdot \left(\xi \vec{\nabla} T \right) + \vec{\nabla} \cdot (\overline{\sigma} \cdot \vec{v}) + W_f + q_H \tag{3.18}$$

Where W_f represents the work of the external volume forces:

$$W_f = \rho \vec{f_e} \cdot \vec{v} \tag{3.19}$$

3.1.5. Turbulence modeling

The conservation equations previously outlined are universally applicable and should fundamentally be used for every convection problem. However, at this stage, it is necessary to distinguish between laminar and turbulent flows. In laminar flows, minor perturbations tend to decrease, maintaining the orderly motion of fluid particles; thus, the flow can be ideally partitioned into adjacent thin layers that can be easily described by relatively coarse grids. Conversely, in turbulent regimes, irregular flows are observed where minor perturbations tend to increase, and fluid particles follow chaotic paths that rapidly change in both space and time. Experimental observations reveal the continuous creation, amalgamation, and dissolution of turbulent eddies across a broad range of characteristic times and lengths. Space-time discretization relies on the smallest and fastest observed eddies to describe the entire range of turbulent fluctuations. Therefore, Direct Numerical Simulation (DNS) of turbulent flows necessitates a substantial number of computational points for mesh design and very short time-steps, resulting in a significant amount of CPU time. Currently, DNS can only be applied to very simple cases due to the limitations in computational capacity.

Given that this approach is not feasible for engineering purposes, alternative models have been proposed to evaluate the effects of turbulent fluctuations without fully simulating the smaller eddies. Large Eddies Simulations (LES) simulate the eddies up to the Kolmogorov scale and model the effects of the smaller, isotropic dissipative eddies. However, this approach is still too CPU-demanding for very large domains, such as those of interest in this work.

A lower level of approximation can be adopted by averaging the transport equations over time to avoid the simulation of the entire range of turbulent fluctuations. This leads to the Reynolds Averaged Navier-Stokes (RANS) equations, which additionally require empirical or semi-empirical information on the turbulence structure and its relation to the averaged variables. The turbulent averaging process is introduced to derive the laws of motion for the mean, time-averaged, turbulent quantities.

For any given quantity A, the following separation

$$A = \overline{A} + A' \tag{3.20}$$

is introduced with:

$$\overline{A}\left(\vec{x},t\right)=\frac{1}{T}\int_{\frac{-T}{2}}^{\frac{T}{2}}\overline{A}\left(\vec{x},t+\tau\right)d\tau \tag{3.21}$$

T represents the time scale, which is selected to be sufficiently large relative to the turbulence time scale, yet still small when compared to other unsteady phenomena. The term $\overline{A}$ denotes the time-averaged quantity, while A' signifies the turbulent fluctuation. When the averaging process is applied to the continuity equation, the following result is obtained:

$$\frac{\partial}{\partial t}\rho+\vec{\nabla}\cdot\left(\rho\vec{\overline{v}}\right)=0 \tag{3.22}$$

When applied to the momentum equations, the subsequent equation for the turbulent mean momentum, in the absence of body forces, is derived as:

$$\frac{\partial}{\partial t}\left(\rho\vec{\overline{v}}\right)+\vec{\nabla}\cdot\left(\rho\vec{\overline{v}}\otimes\vec{\overline{v}}+\overline{p}\overline{I}-\overline{\tau}_V-\overline{\tau}_R\right)=0 \tag{3.23}$$

The relation between the Reynolds stresses, $\overline{\tau}_R$, defined by:

$$\overline{\tau}_{ij}^{R}=-\overline{\rho v_i' v_j'} \tag{3.24}$$

and the mean flow quantities remains unknown. Therefore, the application of the Reynolds-averaged equations to the computation of turbulent flows necessitates the introduction of some modeling of these unknown relations, which is based on theoretical considerations combined with inevitable empirical information.

To solve the RANS equations, a method for calculating these values, often referred to as a "closure technique," is essential. For more comprehensive information about these equations, especially their expanded formulation, references can be made to the ANSYS® Theory Guide [23] and the research conducted by Versteeg and Malalasekera [44]. ANSYS® Fluent provides a variety of models for turbulence.

- **Standard k-ϵ**: This two-equation model is based on transport equations for turbulence kinetic energy (k) and turbulent dissipation rate (ϵ). It was proposed by [41] and assumes that the flow is fully turbulent, with negligible viscous effects. It is commonly used for initial screening solutions.

- **Renormalization-group (RNG) k-ϵ**: This model, proposed by [38], was designed to address certain issues with the standard k-ϵ model. It differs from the standard model in two key ways: it has a slightly different formulation for turbulent viscosity and a modified transport equation for the turbulent dissipation rate (ϵ). This equation was derived from an exact equation for the transport of the mean-square vorticity fluctuation.
- **Realizable k-ϵ**: The term "realizable" indicates that the model satisfies certain mathematical constraints on the Reynolds stresses, consistent with the physics of turbulent flows. According to [38], this model offers several advantages over other k-ϵ models, including more accurate predictions of the spreading rate of both planar and round jets. It is also likely to provide superior performance for flows involving rotation, boundary layers under strong adverse pressure gradients, separation, and recirculation.
- **Standard k-ω**: This empirical model, proposed by [46], is based on transport equations for turbulence kinetic energy (k) and the specific dissipation rate (ω), which is the ratio of ϵ to k. These equations can be integrated throughout the boundary layer down to the wall, resulting in accurate predictions for attached flows.
- **k-ω Shear Stress Transition (SST)**: This model, proposed by [26], is a "hybrid" model that blends the standard k-ϵ model for high Reynolds number regions and the standard k-ω model for low Reynolds number regions. This combination leverages the advantages of both models, making it suitable for a broader range of fluid flows.

All these turbulence models have been used in recent studies. To the author's knowledge, the most similar work to this is that of [30], who focused on the interaction between methane jets and the ground. The author tested four turbulence models and found that the k-ω SST model provided the best solution for impinging jet problems.

3.1.6. k-ω Shear Stress Transition (SST)

To address the closure issue, an appropriate turbulence model must be employed to model the terms in the Reynolds Stress Tensor [31]. Over the past three decades, numerous models have been developed, among which the k-ω SST model was selected for this study. This model is a two-equation eddy-viscosity model that utilizes the k-ω formulation in the boundary layer, making it applicable through the viscous sub-layer down to the wall. As such, the k-ω SST model can be considered a Low-Re turbulence model without the need for additional damping functions.

The k-ω SST model also features an advanced near-wall treatment that automatically transitions from the low to the high Reynolds number ω formulation. Furthermore, the SST equations can switch to a k-ϵ form in the free-stream, circumventing the common issue of the k-ω model being overly sensitive to the inlet free-stream turbulence properties.

The selection of the k-ω SST model is justified by its reported effectiveness in handling High-Pressure Jets [28, 30]. Additionally, the SST model can perform a "hybrid" modelling of turbulence, employing a k-ω model near the walls and a k-ϵ model for the free-stream region of the flow [23, 26, 44].

3.1.7. Near-wall approach

Turbulent flows can be significantly influenced by the presence of walls, as noted by [3, 10]. The no-slip condition, which must be satisfied at the wall, impacts the mean velocity field.

The near-wall region of the fluid is where significant gradients in fluid characteristics occur, and where momentum and other scalar transports are most pronounced. This region can be divided into three distinct layers. The innermost layer, known as the "viscous sublayer," is almost laminar, with viscosity playing a dominant role in momentum and heat or mass transfer. The outer layer, referred to as the "fully turbulent layer," is primarily influenced by turbulence. Between these two layers is a middle region where the effects of viscosity and turbulence are equally significant.

The numerical simulation of these processes presents two key challenges:

- Accounting for viscous effects at the wall.
- Resolving the rapid variation of flow variables within the boundary layer region.

These subdivisions of the near-wall region are illustrated in Figure 3.1.

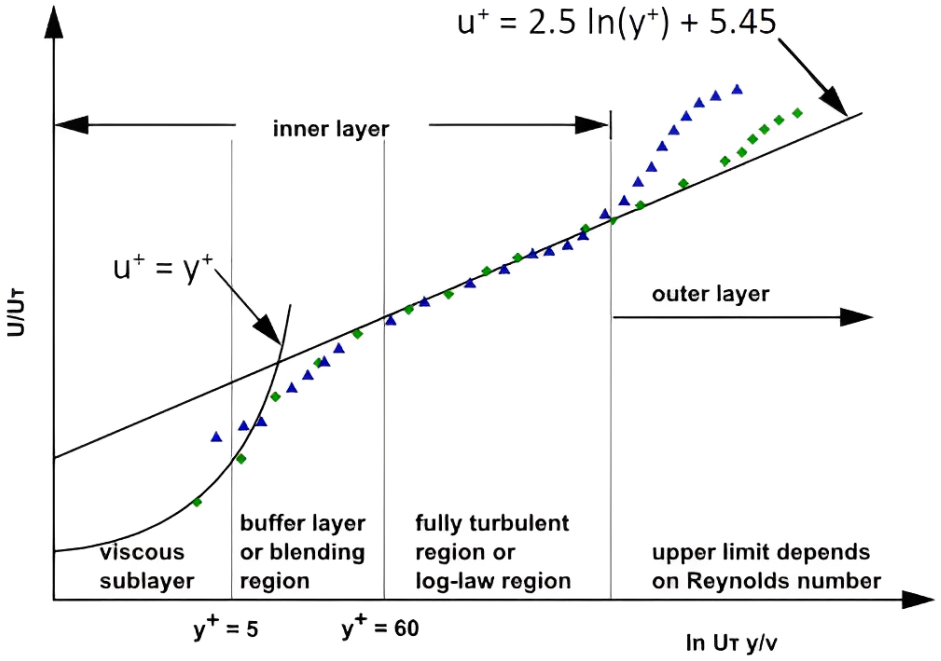

Figure 3.1: Boundary Layer description.

As depicted in Figure 3.1, a dimensionless velocity, denoted as u_τ, and a dimensionless wall distance, represented as y^+, can be employed to provide a dimensionless characterization of the near-wall region. These quantities are computed as follows:

- $u_\tau = \sqrt{\frac{\tau_{wall}}{\rho}}$
- $y^+ = \frac{yu_\tau}{\nu}$

Generally, there are two possible approaches to model the near-wall region:

- Near-Wall Model
- Wall Function

In the "Near-Wall Model approach", modifications are made to the turbulence models to facilitate the use of the mesh extending to the wall, thereby solving for the zone affected by viscosity, inclusive of the viscous sublayer.

Conversely, the Wall Function approach does not resolve the viscous sublayer and the buffer layer. In these regions, semi-empirical formulas are employed to convey the viscous effects from the wall to the fully turbulent region, as depicted in Figure 3.2.

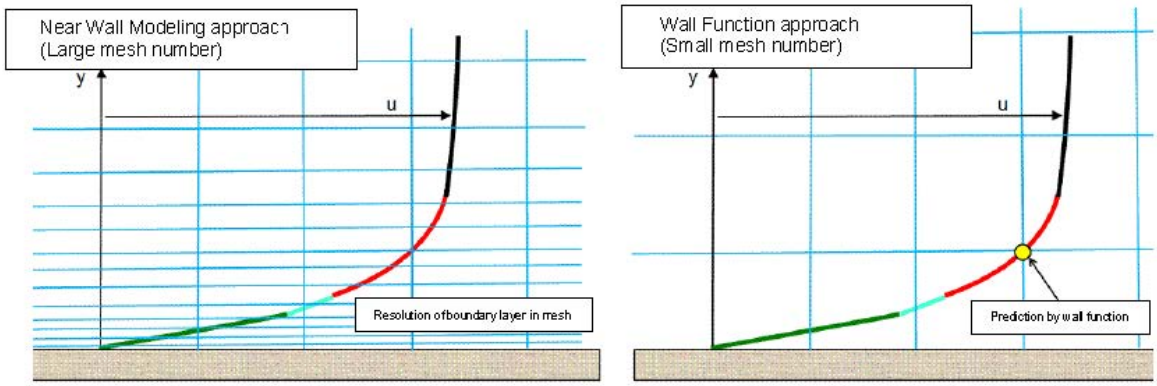

Figure 3.2: Mesh for the two Near-wall approaches [10].

3.1.8. Birch's Equivalent Diameter Approach

There are various methodologies to model the source of high-pressure under-expanded jets, which span from computationally demanding solutions that resolve the jet's shock structure to simpler formula-based approaches, such as pseudo-source or notional nozzle methods.

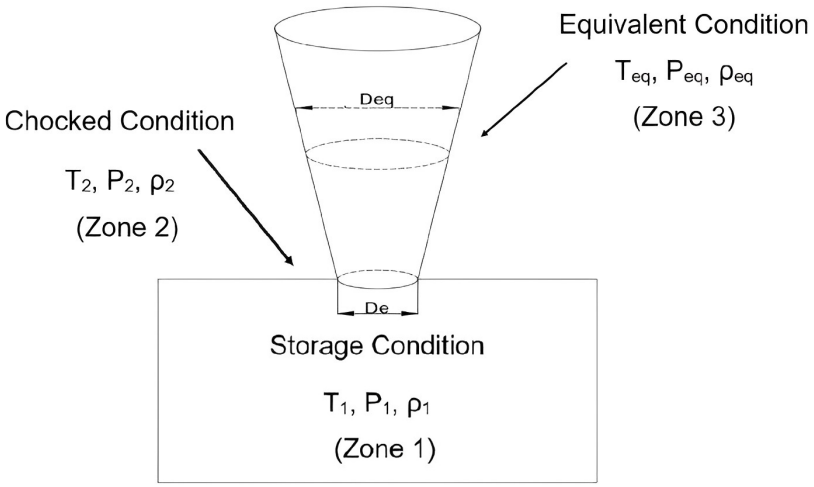

Figure 3.3: Equivalent Diameter Approach [4].

The equivalent diameter approach relies on the mass conservation, under the assumption of no entrainment of ambient air. This approach involves a hypothetical point ahead of the exit plane where the flow is assumed to have the same pressure and temperature as the ambient fluid and to be at sonic velocity.

This assumption allows for the bypassing of any modeling of the initial zone of the supercritical jet, where shock-waves are present. According to the mass conservation hypothesis between the original orifice (zone 2 in Figure 3.3) and the pseudo-orifice (zone 3 in Figure 3.3), it is possible to write, as defined in the work by [4]:

$$V_{eq} = \sqrt{\frac{\gamma R T_{eq}}{M_w}} \tag{3.25}$$

$$\rho_{eq} = \frac{P_{eq}}{R T_{eq}} \tag{3.26}$$

$$T_{tot} = T_{eq} + \frac{V_{eq}^2}{2 * C_p} \tag{3.27}$$

It is assumed that the equivalent temperature is equal to the ambient one, and the equivalent pressure is equal to the ambient one.

$$T_{eq} = T_{\infty} \tag{3.28}$$

$$P_{eq} = P_{\infty} \tag{3.29}$$

where,

- V_{eq} is the velocity at the Equivalent Diameter.
- γ is the heat capacity ratio.
- R is the universal gas constant.
- M_w is the molecular weight.
- ρ_{eq} is the density at the Equivalent Diameter.
- T_{eq} is the temperature at the Equivalent Diameter.
- P_{eq} is the pressure at the Equivalent Diameter.
- C_p is the specific heat capacity at constant pressure.
- T_{tot} is the Stagnation temperature.

The Equivalent Diameter is computed as

$$d_{ps} = d\sqrt{C_d \frac{V_2}{V_{eq}} \frac{\rho_2}{\rho_{eq}}} \tag{3.30}$$

where

- V_2 is the velocity in the zone 2, as shown in Figure 3.3 .
- C_d is the discharge coefficient.
- ρ_2 is the density at zone 2.
- d is the real diameter of the source.

3.1.9. ANSYS® Simulation Software

Computational Fluid Dynamics (CFD) is a powerful tool that enables engineers and scientists to simulate the interaction of flows with complex surfaces and predict fluid behavior in various scenarios. CFD offers a cost-effective, safe, and efficient method to test hypotheses and examine scenarios that could be difficult, dangerous, or impossible to study experimentally. A pivotal role in the successful execution and accurate analysis of CFD simulations is played by the software employed. The ANSYS® 2022 software suite, a comprehensive and integrated platform, stands out as a leader in this field. The suite comprises several dedicated software tools, each fulfilling a unique and indispensable role in the overall process.

- **ANSYS® Workbench** acts as a robust and dynamic interface, providing an integrated environment for leveraging the power of various other software tools within the suite. It coordinates the functioning of these tools, facilitating their synergistic utilization for a smooth and efficient workflow. Through its project schematic feature, ANSYS® Workbench enables users to build and manage complex simulations, ensuring that every step of the process, from geometry design to results visualization, is efficiently connected and seamlessly executed.
- **ANSYS® SpaceClaim**, another crucial component of the suite, is a 3D modeling tool responsible for designing the geometries of the various scenarios under study. This direct modeling software allows for the easy creation, modification, and simplification of complex geometries, which forms the foundation of CFD simulations. SpaceClaim's user-friendly interface and powerful capabilities significantly enhance the flexibility and speed of geometry preparation, making it a vital asset in the

initial stages of simulation.

- **ANSYS® Fluent Meshing** has been fundamental for the creation of a suitable mesh for each scenario. This dedicated meshing software tool is capable of handling complex geometries and offers a wide range of meshing options, from simple tetrahedral to high-quality polyhedral and hexahedral meshes. Fluent Meshing ensures an optimal balance between computational efficiency and simulation accuracy by controlling mesh resolution in areas of interest. Its advanced meshing capabilities are critical for accurately capturing fluid behavior and ensuring the reliability of simulation results.

- **ANSYS® Fluent** is the software responsible for addressing CFD problems. It is a state-of-the-art solver, which offers a wide range of physical models to capture the complexities of fluid dynamics, heat transfer, and chemical reactions. Fluent's robustness, accuracy, and speed are instrumental in tackling complex CFD simulations, from turbulent flows to multiphase and reacting flows. By leveraging parallel processing capabilities, Fluent provides swift and accurate solutions, making it an indispensable component of the CFD simulation process.

- **ANSYS® CFD-Post**, finally, is employed for the post-processing phase. This tool is specifically designed to efficiently analyze and visualize the simulation results obtained from Fluent. With an array of visualization options, including contour plots, vector plots, and pathlines, CFD-Post enables users to gain a deeper understanding of fluid behavior and extract meaningful insights from the simulation data.

  To summarize, each component of the ANSYS® 2022 software suite plays a distinct and crucial role in the execution of CFD simulations. From the initial steps of geometry design and meshing to solving the complex CFD processes and visualizing the results, the ANSYS® suite provides a comprehensive, integrated, and efficient platform for successfully carrying out CFD studies.

3.2. Analytical approach

3.2.1. The CSTR model

In the course of this research, a comprehensive and detailed analysis was conducted, central to which was the creation of an extensive Microsoft Office Excel worksheet. This worksheet served as a repository for a multitude of case study scenarios, that will be better investigated later, based on mirror real-world situations. The physical data for these elaborations was taken from a third-party software known as PHAST, a renowned tool in the field of safety analysis.

The data provided by PHAST includes a wide array of parameters, each one integral to the comprehensive understanding of the scenarios at hand.

These parameters are, specifically:

- The diameter of the rupture hole: this parameter provided insight into the size of the potential leak, a crucial factor in understanding the severity of the scenario.
- The input temperature and pressure: these parameters were essential in determining the initial conditions of the system.
- The peak release pressure of the hydrogen and methane mixture: this parameter offered a measure of the maximum pressure exerted by the mixture upon release.
- The velocity of the jet: this parameter provided a measure of the speed at which the mixture was expelled.
- The upper and lower flammable limits (UFL and LFL): these parameters defined the concentration boundaries within which the mixture could ignite, thus providing a measure of the flammability risk.

In this study, the Continuous Stirred-Tank Reactor (CSTR) model was adapted to meet the specific requirements of the scenario. While no reactions were considered in this model, the accumulation of the mixture over time was taken into account. This was a crucial aspect of the model as it allowed for the tracking of the concentration of the mixture in the identified volume over time.

In the adapted CSTR model, the balance equation was formulated to measure the concentration of the hydrogen-methane mixtures within the defined control volume. The CSTR model is a well-established model in the field of chemical engineering, renowned for its

ability to simulate systems where a reaction, or in this case, an accumulation, occurs within a well-mixed environment. The balance equation, a fundamental component of the CSTR model, was carefully constructed to accurately represent the dynamics of the system.

The inlet flowrate term of the balance equation was represented by the sum of two components: the inlet flowrate of the naturally ventilated air and the flowrate of the released hydrogen-methane mixture entering the control volume. This combination of flowrates accurately represented the total influx of substances into the system.

The outlet flowrate term in the balance equation was designed to account for the sum of the well-mixed flowrates exiting the control volume. This term ensured that the balance equation accurately represented the total outflow of substances from the system.

The accumulation term in the balance equation was specifically designed to account for the increasing concentration of the hydrogen-methane mixture within the control volume over time. This term was crucial in tracking the evolution of the mixture's concentration within the system, providing valuable insights into the behavior of the system over time.

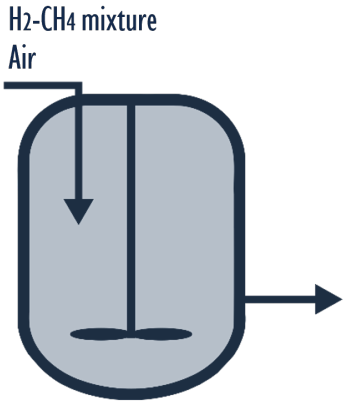

Figure 3.4: A simple qualitative representation of the model.

The adaptation of the CSTR model in this study allowed for a comprehensive analysis of the behavior of the hydrogen-methane mixtures under various scenarios. The careful construction of the balance equation, with its specific inlet, outlet, and accumulation terms, provided a robust framework for tracking and understanding the dynamics of the system. The following assumptions had to be made to fit the model:

- Perfect mixing: this assumption negated any spatial gradients of concentration within the system, thus simplifying the model by assuming a uniform concentration throughout.

- Defined control volume: this assumption allowed for the system to be isolated and studied independently of its surroundings.
- Constant fluid density: this assumption simplified the model by negating any changes in density that might occur due to changes in concentration.

The data supplied by PHAST was used to calculate two crucial aspects of the model: the release flux and the natural ventilation inlet flux. The release flux provided a measure of the rate at which the mixture was being released into the system, while the natural ventilation inlet flux provided a measure of the rate at which fresh air was entering the system. These values were then used to determine the total inlet flux for the balance, a crucial component in understanding the dynamics of the system.

With these calculations, it was possible to estimate the concentration of the studied mixture inside the control volume over time. This was a crucial aspect of the study as it allowed for the tracking of the concentration of the mixture within the system, providing valuable insight into the behavior of the system over time.

The data was further processed to generate concentration profiles over time. These profiles allowed for the monitoring of the concentration evolution of the mixture. The upper and lower flammability limits were taken into consideration in these profiles, which helped in defining the flammability window in time for various mixtures. This was done for each hydrogen-methane composition considered in the study and for each scenario.

This comprehensive approach allowed for a thorough understanding of the behavior of the hydrogen-methane mixtures under different conditions. The use of an Excel worksheet facilitated the organization and analysis of the data, making it a valuable tool in this study.

3.2.2. The GAME Project

The Guidance for the Application of the Multi-Energy Method (GAME) project is a comprehensive initiative that aims to address the existing challenges in the application of the Multi-Energy Method (MEM). The MEM is a relatively straightforward and practical approach used to determine the blast parameters from a vapor cloud explosion, with a particular focus on the released overpressure. However, the application of MEM has been limited due to insufficient guidance on the selection of the source strength. The GAME project was undertaken to provide this much-needed guidance.

The GAME project aims to enhance the practicality and effectiveness of the MEM by

providing comprehensive guidance on the selection of the source strength. This guidance is expected to facilitate more accurate and reliable determinations of blast parameters, thereby improving the safety and risk management of operations involving the potential for vapor cloud explosions.

The project is grounded in rigorous scientific research and leverages advanced computational methodologies to calculate the energy released in different scenarios. The calculated energy is a key parameter that is used to determine the magnitude of the explosion radius, a critical factor in assessing the potential impact and damage of a vapor cloud explosion.

The GAME project also addresses several complex scenarios that can arise in the application of the MEM. For instance, the project provides guidance on how to handle situations where the ignition location is not at the center of the obstacle configuration, or where the obstacle configuration is partially filled with a flammable mixture. The project also provides guidance on how to handle situations where the aspect ratio of the obstructed region is not equal to one, which can affect the choice of the path length (Lp) used in the MEM.

Furthermore, the GAME project acknowledges the influence of differently shaped obstacles on the explosion progress. The project proposes a practical approach to handle non-cylindrical obstacles by representing them as cylinders with a length equal to the largest dimension of the obstacle and a cross-section area equal to the cross-section area of the obstacle. However, the project also acknowledges that the physical correctness of this procedure is not yet clear, particularly for flat plates [45].

For what concerns the released overpressure, The data that was processed and analyzed was derived from the PHAST software. This software is a comprehensive hazard analysis tool used for evaluating the potential hazards posed by industrial processes, particularly those involving the release of hazardous substances.

Overpressure, which corresponds to the pressure caused by the shock wave over and above the normal atmospheric pressure is a crucial because, as already mentioned, it directly influences the magnitude of the explosion radius. The explosion radius, conversely, is a key determinant of the extent of damage that can be caused by an explosion. Therefore, accurately determining the overpressure parameters is of high importance in predicting and mitigating the potential damage caused by an eventual explosion.

In this analysis, several indicative cases were considered, to have a tangible outline of the real possible outcomes. These cases were chosen based on their known pressure thresholds necessary to cause specific types of damage. By studying these cases, we can gain a better

understanding of the relationship between overpressure, explosion radius, and the resulting damage.

The first case considered was the failure of reinforced concrete structures (300 mbar). Reinforced concrete, which is concrete embedded with steel bars for increased strength, is commonly used in industrial structures due to its durability and resistance to fire and weathering. However, these structures can fail under extreme overpressure conditions, leading to catastrophic consequences.

The second case involved the failure of steel structures (170 mbar). Steel, being a robust and versatile material, is widely used in various industrial applications. However, like reinforced concrete, steel structures can also fail when subjected to high overpressure, leading to significant damage.

The third case focused on glass breakage (20 mbar). Glass, while not as robust as concrete or steel, is commonly used in industrial settings, particularly in windows and certain equipment. Glass breakage can occur at relatively lower overpressure levels compared to concrete or steel, and can result in injuries and secondary damage due to flying debris.

Overpressure is correlated to a specific set of parameters which are fundamental to characterize the environment where the vapor cloud is situated, as well as the properties of the vapor cloud itself. In scenarios where there is low ignition energy and no confinement, which can be described as open or three-dimensional (3D) conditions it is possible to use the following specific expression:

$$P_0 = 0.84 * (VBR * L_p/D)^{2.75} * S_L^{2.7} * D^{0.7} \tag{3.31}$$

where

- P_0 is the maximum explosion overpressure [bar].
- VBR is the volume blockage ratio.
- L_p is the length of the flammable path [m].
- D is the typical diameter [m].
- S_L is the laminar burning velocity of the flammable mixture [m/s].

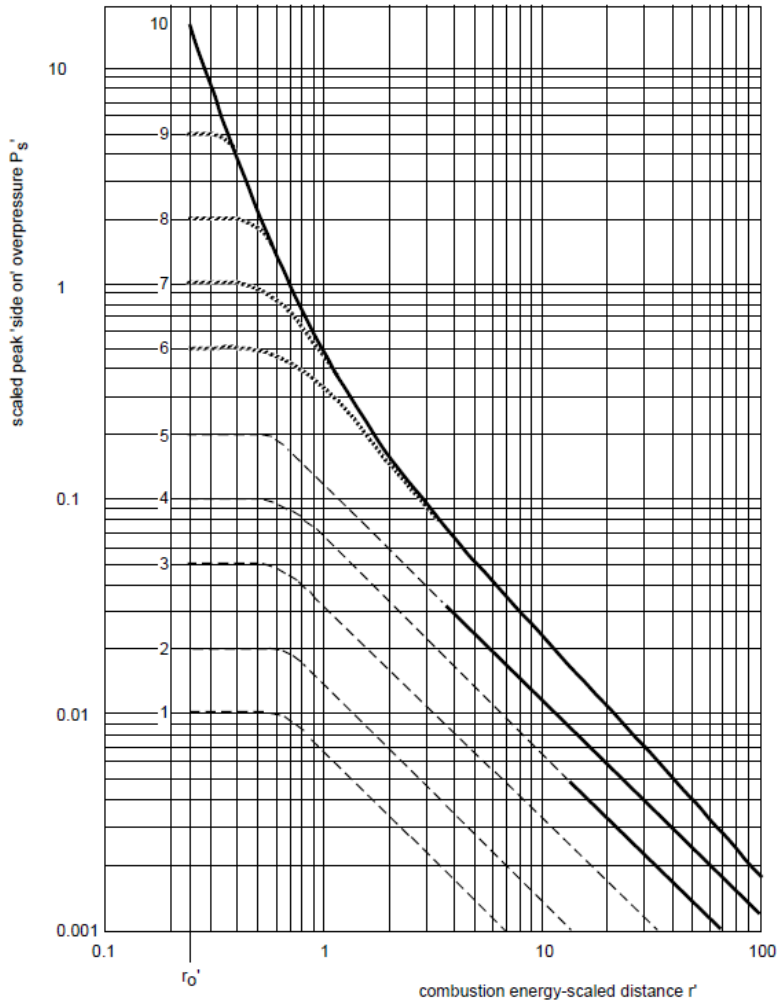

Figure 3.5: Blast chart MEM for overpressure [45].

The Figure 3.5 presents the blast chart associated with the Multi-Energy Method (MEM). The purpose of this chart is to facilitate the determination of the peak blast overpressure, denoted as P_s, at a specific distance, denoted as r, from the epicenter of the explosion, considering a certain total combustion energy E. To achieve this, a calculation of the scaled distance, denoted as r', is required:

$$r' = \frac{r}{(\frac{E}{p_0})^{\frac{1}{3}}} \tag{3.32}$$

The blast chart provides a value for the scaled blast overpressure, denoted as P'_s. The actual blast overpressure, P_s, can then be obtained by multiplying the scaled blast overpressure, P'_s by p_0, the ambient overpressure.

The overpressure in the explosion, denoted as P_0, plays a crucial role in determining the

appropriate line to follow on the blast chart. Specifically, for scaled distance values that are smaller than r'_0, the pressure P_0 guides the selection of the correct overpressure at the required scaled distance [45].

4 | Discussion and Results

4.1. Scenarios

In the next paragraph, a detailed exploration of four scenarios considered relevant to the study will be carried out. These selected scenarios are essential for the subsequent analytical and CFD and analytical calculations. Their role is pivotal in unveiling the shades of the study and facilitating a comprehensive understanding of the identified phenomena.

The three-dimensional (3D) geometric structures utilized within the context of these scenarios were created utilizing the sophisticated capabilities of the ANSYS® SpaceClaim CAD software. The significance of 3D modeling in our exploration cannot be understated, as it grants us the ability to visualize, simulate, and thereby comprehend the mechanics involved in a more intricate and detailed manner. The use of ANSYS® SpaceClaim, warrants a special mention. Its user-friendly features and robust capabilities have made it an indispensable tool in our investigation, enabling the creation of intricate 3D geometries with relative ease and precision.

This chapter, therefore, represents a synthesis of carefully chosen scenarios, state-of-the-art analytical methods, and pioneering software tools, all working in concert to illuminate our research questions. As the reading progresses, a more profound comprehension of the significance and the interrelation of these scenarios within the context of the current inquiry will be attained. For the dimensioning of the models, please refer to Appendix A.

4.1.1. Scenario 1

The first studied scenario takes into consideration the unintended discharge originating from a subsurface conduit. This occurrence is chiefly triggered by accidental interference resulting from operations conducted by an external party. Illustrative examples of such activities could encompass undertakings such as excavation processes, amongst other comparable actions. It has been hypothesized that the release emanating from the pipeline might be best approximated, for calculation purposes, as a discharge from the ground surface level within a confined volume. This supposition has been adopted to facilitate a

detailed examination of the effects exerted by the immediate presence of the cloud.

The subsequent scenario is posited to transpire within the confines of an urban landscape.This assumption is essential as the urban context can influence the extent and consequences of the said discharge due to various factors like population density, the proximity of buildings, and the presence of underground utility networks.

Further to this, it is hypothesized that the outflow is characterized by a condition referred to as 'full pipe flow'. This implies that the release transpires with the conduit being entirely filled, thereby suggesting a significant and potentially problematic discharge. This condition underlines the severity of the event and calls for appropriate cautionary measures during third-party operations in the vicinity of such infrastructures.

With respect to the specific case being discussed, it is significant to point out that exclusively an analytical study has been carried out. This choice has been informed by the relative simplicity of the scenario, which did not necessitate more complex investigative tools. Consequently, the employment of Computational Fluid Dynamics (CFD) calculations, often reserved for more intricate situations, has been deemed unnecessary in this instance.

4.1.2. Scenario 2

This scenario involves an accidental emission from a pressure reduction facility (Digitized Final Reduction Groups, GRFD), occurring in a urban environment. This accidental release could be triggered by external mechanical influences, like the impact resultant from a vehicular mishap.

The primary objective of this examination is, as well as in the first and the next scenarios, to investigate the implications of different concentrations of Hydrogen (H2) within the blend of Natural Gas and Hydrogen (NGH2).

This investigation becomes crucial as increasing H2 levels could significantly influence operational and safety parameters.

The varying concentrations of hydrogen in the assumed Natural Gas and Hydrogen (NGH2) blends call for significant attention and consideration. These changes in hydrogen composition could play a crucial role in the overall risk assessment within the context of this scenario.

Furthermore, it is also within the scope of this study to consider and evaluate the require-

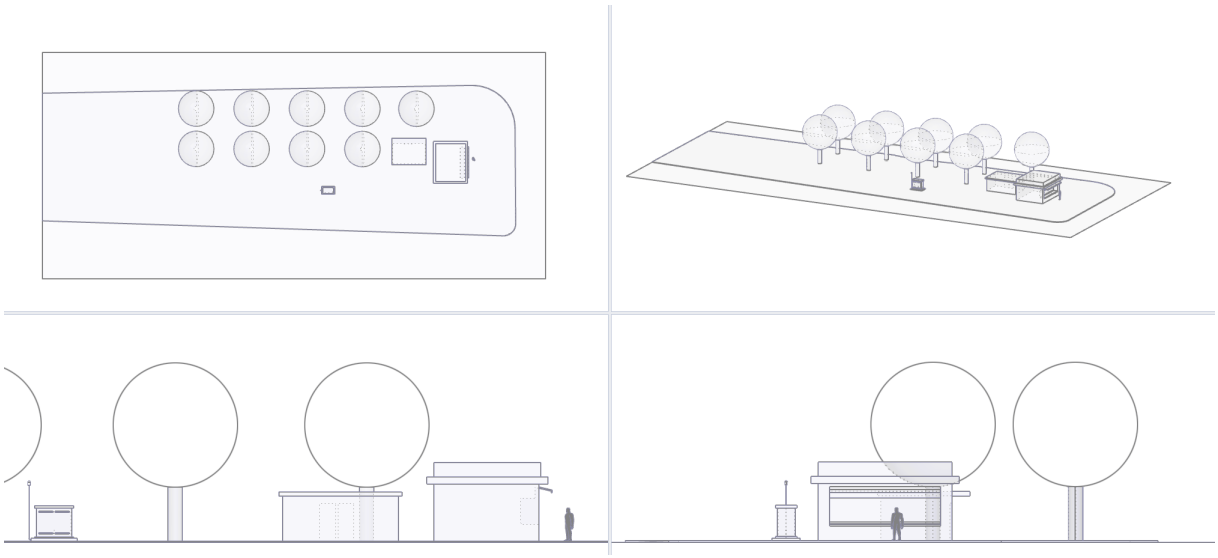

Figure 4.1: Perspective drawing of Scenario 2.

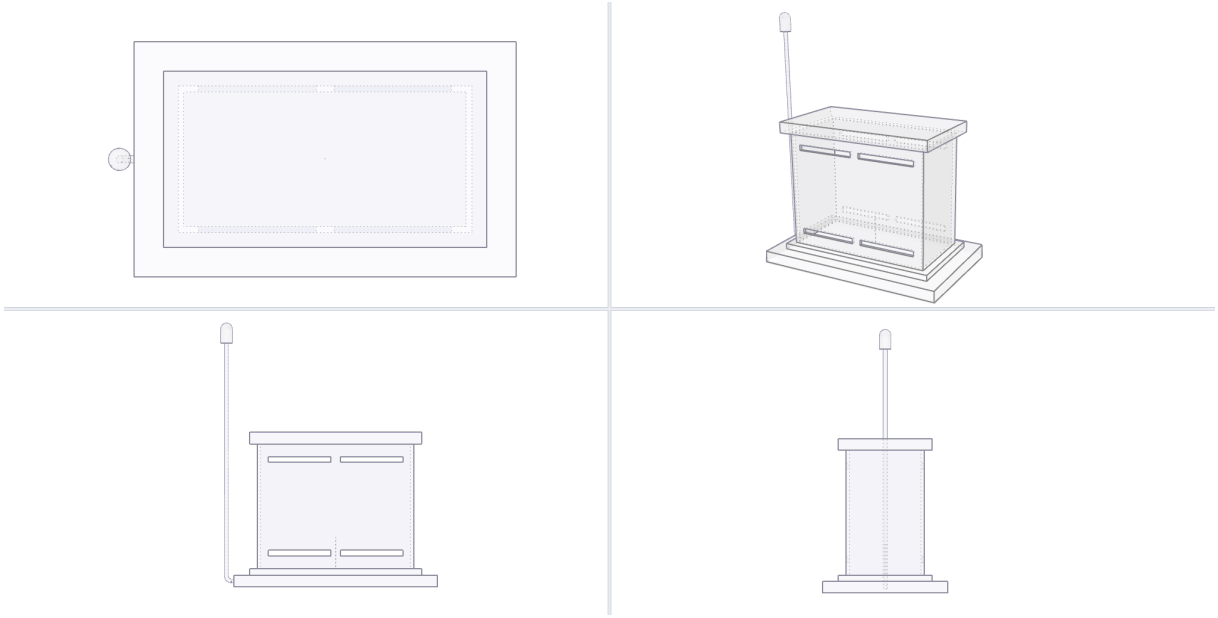

Figure 4.2: Detail of the GRFD cabin in Scenario 2.

ment of any additional safety barriers or precautions. This ensures that any necessary protective measures are identified and implemented, therefore enhancing the overall safety of the operation and surrounding environment.

4.1.3. Scenario 3

This discussion is primarily focused on an unexpected event within a structure known as a REMI cabin (from italian "REgolazione e MIsura"). This cabin functions as a regulation and measurement plant, representing a critical delivery point within the gas distribution network. Its primary functions include the decompression and measurement of natural gas. The REMI cabin contains a variety of sophisticated instruments, designed to facilitate several significant processes in the distribution system.

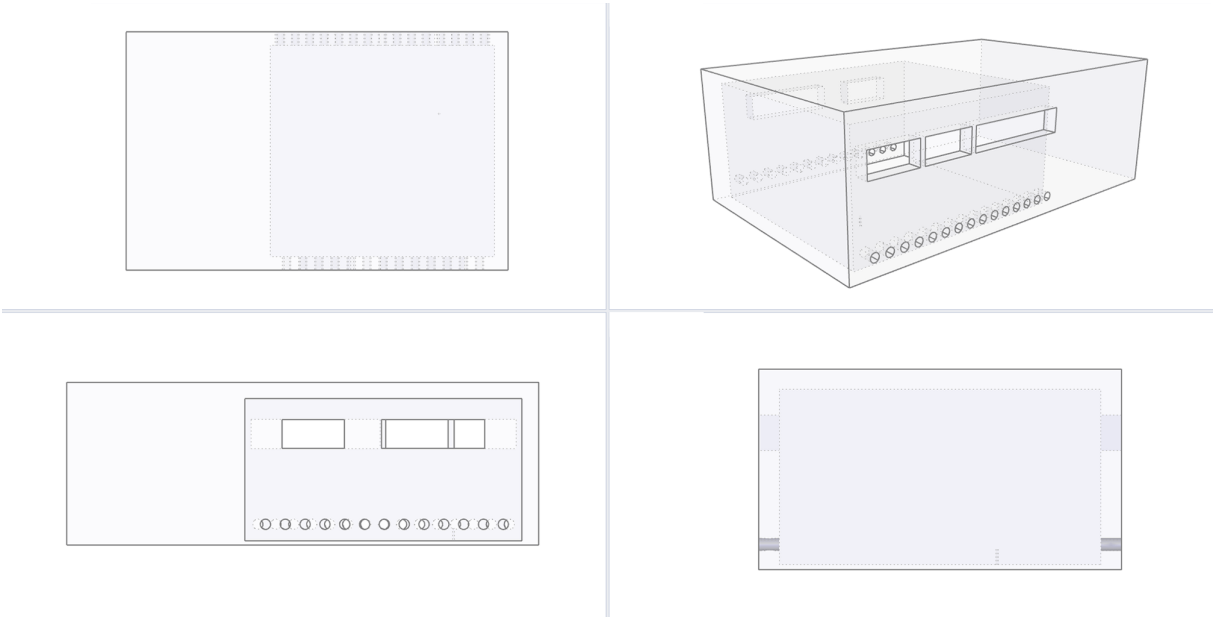

Figure 4.3: Perspective drawing of Scenario 3.

An unexpected event that may eventually occur within this cabin is mainly triggered by the malfunction of a flanged coupling, the formation of a crevice as a result of corrosion, or other incidental occurrences. These events share a distinctive characteristic, a rupture that is comparatively small, with its size not exceeding 10% of the diameter of the connection in question.

The main aim of this study is to look into the chance of explosive and flammable mixtures forming in such a space-limited environment. The variations in H2 concentrations may, also in this case, drastically modify the characteristics of the released mixture, potentially amplifying its explosiveness or combustibility. Comprehending this dynamism helps in framing appropriate safety protocols and standards, which could ensure the prevention of explosive or fire hazards in such confined environments, thereby augmenting overall safety measures and safeguarding both the infrastructure and personnel involved.

4.1.4. Scenario 4

This scenario concerns an accidental discharge within an underground well associated with the Digitized Final Reduction Groups (GRFD), originating from a reduction facility located in an urban environment. This discharge can be attributed primarily to the malfunctioning of a flanged coupling, the occurrence of a crack due to corrosion, or other incidental events. These incidental events share a common characteristic, which is the manifestation of a rupture with an equivalent diameter that is considerably small, with the maximum limit not exceeding 10% of the diameter of the implicated connection.

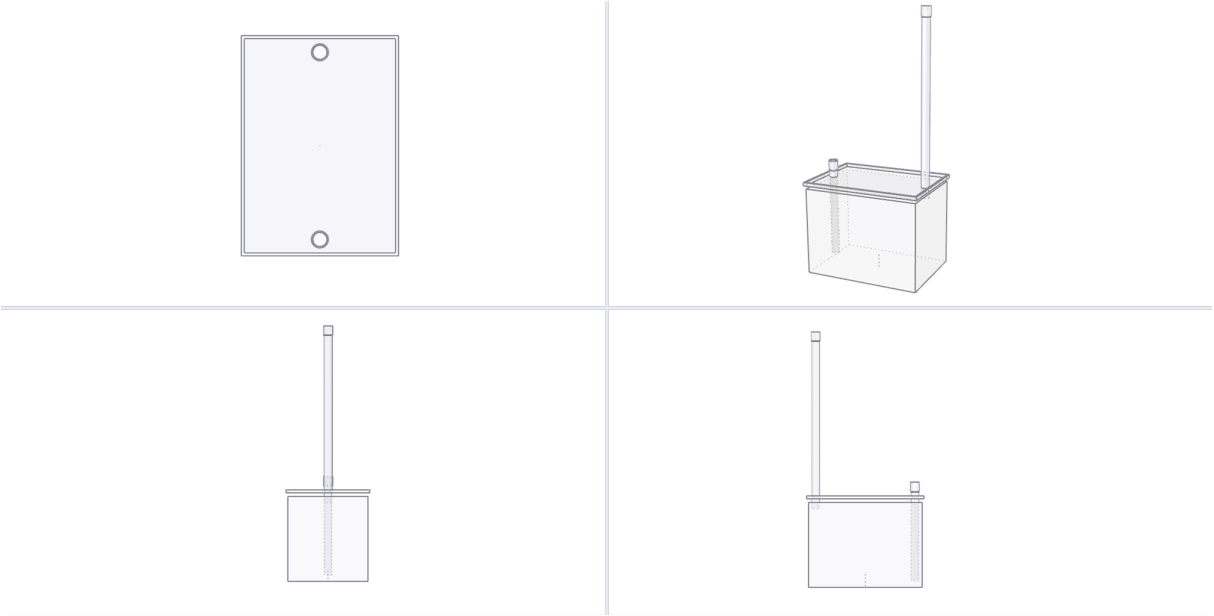

Figure 4.4: Perspective drawing of Scenario 4.

As in the previous instances examined in this study, the central objective here is to analyze the potential for the formation of explosive and flammable mixtures within this confined space. This analysis is of critical importance as the proportion of Hydrogen (H2) in the Natural Gas and Hydrogen (NGH2) blend undergoes variations. This fluctuating concentration of H2 can significantly alter the properties of these potentially hazardous mixtures, thereby impacting the safety parameters within the underground well of the GRFD.

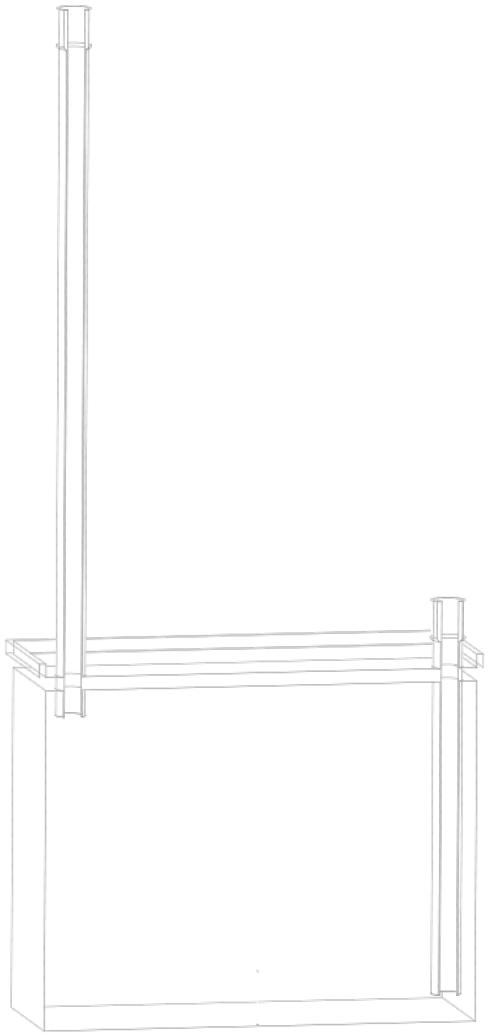

Figure 4.5: Section of Scenario 4 geometry in detail.

As previously stated, also this particular scenario contributes to have a comprehensive understanding of the implications of varying H2 concentrations within the NGH2 mixture in confined spaces. The investigation thus forms an integral part of the broader effort to enhance the safety measures.

4.2. Scenario data and parameters

The following table (Table 4.1) presents the initial parameters that have been defined for the upcoming calculations. These are correlated to the four scenarios that have been previously examined.

	Scenario 1	*Scenario* 2	*Scenario* 3	*Scenario* 4
Control Volume	7.5 m^3	3.84 m^3	313.108 m^3	20.808 m^3
Hole diameter	80 mm	8 mm	8 mm	8 mm
Pressure	12 bar	5 bar	75 bar	50 bar
Temperature	20°C	20°C	20°C	20°C
Air Flowrate	0.010656 m^3/s	0.0529 m^3/s	0.785 m^3/s	0.010656 m^3/s

Table 4.1: Defining parameters of the different scenarios.

Before diving deeper into the discourse, it becomes crucial to identify the specific concentrations that have been opted for in the different Natural Gas and Hydrogen (NGH2) blends. Along with this, the relative peak flowrates determined through the use of the software PHAST also needs to be specified (Table 4.2).

The list provided below enumerates the various instances of mixtures with different hydrogen molar compositions that will be addressed in the course of this study:

1. NGH2 blend with 0% molar oxygen composition.
2. NGH2 blend with 10% molar oxygen composition.
3. NGH2 blend with 20% molar oxygen composition.
4. NGH2 blend with 40% molar oxygen composition.
5. NGH2 blend with 100% molar oxygen composition.

These compositions have been chosen in order to provide a situation where a quantity of hydrogen that is less than that of methane is introduced into the pipelines, and to compare it with the extreme cases where only hydrogen or only methane are present.

As for the weather/wind conditions, for what concerns the gas dispersion modelling in PHAST, the category D5 has been chosen. The D5 designation refers to a specific set of

atmospheric stability conditions often used in dispersion modeling studies, including those involving the dispersion of hazardous materials in the air. It's a classification from the Pasquill-Gifford stability classes, which rank from A (very unstable) to F (very stable). The "D" class indicates neutral atmospheric stability, and the "5" refers to a wind speed of 5 m/s [9]. The computations that will be carried out and taken into account from now on are based on this consideration.

Molar H_2 %	*Scenario* 1	*Scenario* 2	*Scenario* 3	*Scenario* 4
0%	9.84023 kg/s	0,0443951 kg/s	0,622403 kg/s	0,405610 kg/s
10%	9.38740 kg/s	0,0424155 kg/s	0,582884 kg/s	0,383010 kg/s
20%	8.91738 kg/s	0,0403449 kg/s	0,545578 kg/s	0,360759 kg/s
40%	7.90854 kg/s	0,0358572 kg/s	0,473471 kg/s	0,315831 kg/s
100%	3.49518 kg/s	0,0158911 kg/s	0,203741 kg/s	0,137276 kg/s

Table 4.2: Release peak flowrates in the different cases.

Moreover, the Table 4.3 presents the Lower Flammability Limit (LFL) and Upper Flammability Limit (UFL) values for the blend composed of air, methane, and hydrogen, illustrating how these values vary according to variations in the hydrogen composition in terms of volumetric concentration.

	0% H_2	20% H_2	30% H_2	40% H_2	100% H_2
LFL	0.044	0.044	0.043	0.042	0.040
UFL	0.165	0.179	0.195	0.240	0.750

Table 4.3: Flammability limits [vol/vol] for the different blends.

4.3. CSTR model approach

4.3.1. Flammability windows

Based on the previously obtained Lower Flammability Limit (LFL) and Upper Flammability Limit (UFL) data, it has been feasible to frame the concentration profile of the NGH2 mixture within a specific temporal window. As previously mentioned, these profiles were calculated based on the Continuous Stirred-Tank Reactor (CSTR) model, using the formula 4.1, which is the characteristic formula for the concentration profile of a CSTR that features an accumulation term and lacks a reaction term.

In this formula, Q is the volumetric flow rate of air - this includes the inflow rate of air due to natural ventilation, which is provided as initial data, combined with the volumetric flow rate of the mixture released into the control volume. Finally, V stands for the control volume, and t represents the specific point in time under consideration.

$$C_{mix}(t) = C_{mix}^{IN}\left(1 - e^{-\frac{Qt}{V}}\right) \tag{4.1}$$

Therefore, a decision was made to convert the LFL and UFL values into percentage terms, in order to provide an appropriate comparison among the different cases. This conversion defines a temporal flammability window ranging from 0% (LFL) to 100% (UFL). The relative proportional concentration profile was calculated as it follows in formula 4.2.

$$C_{mix}^{\%}(t) = \frac{C_{mix}(t) - LFL}{UFL - LFL} \tag{4.2}$$

The forthcoming plots depict the profile of the aforementioned concentration over time, measured in seconds, within the previously mentioned flammability window.

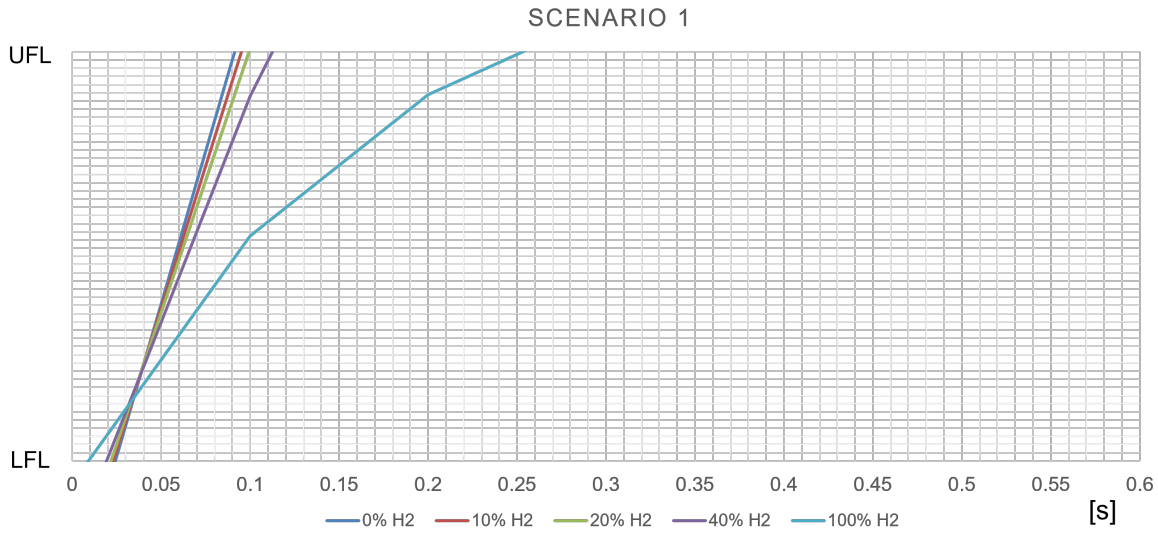

Figure 4.6: Flammability window in Scenario 1.

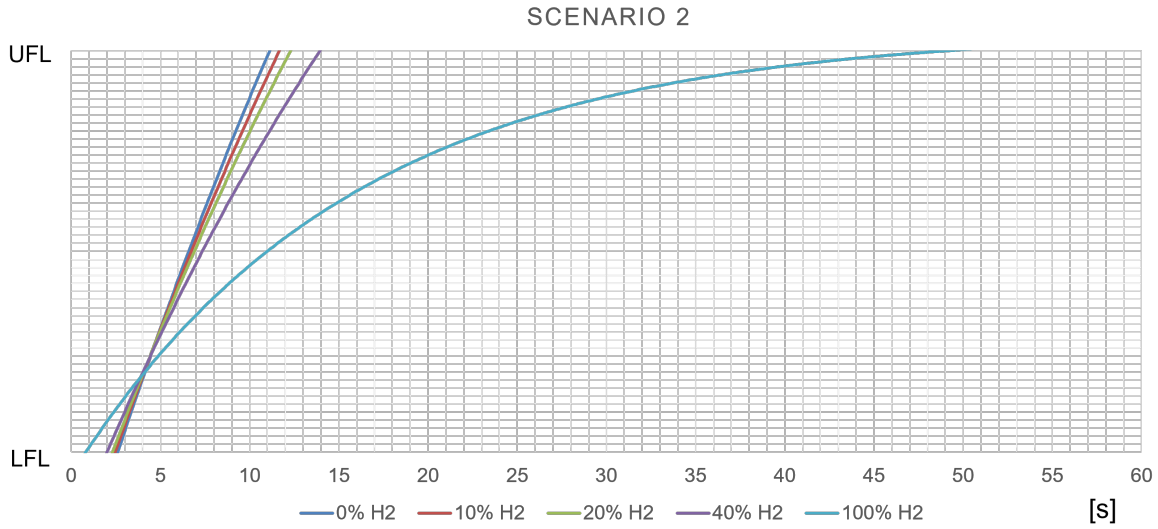

Figure 4.7: Flammability window in Scenario 2.

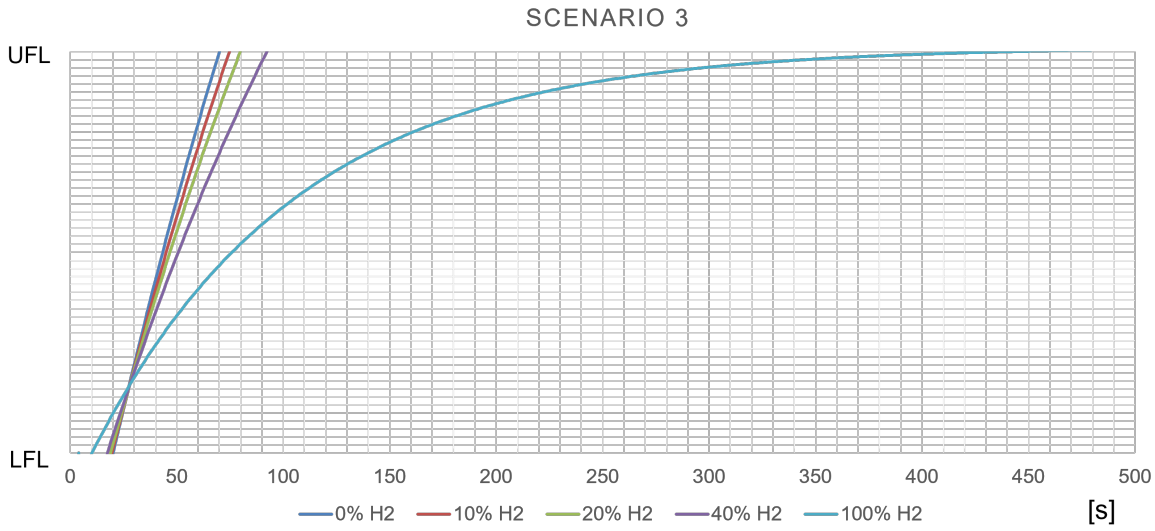

Figure 4.8: Flammability window in Scenario 3.

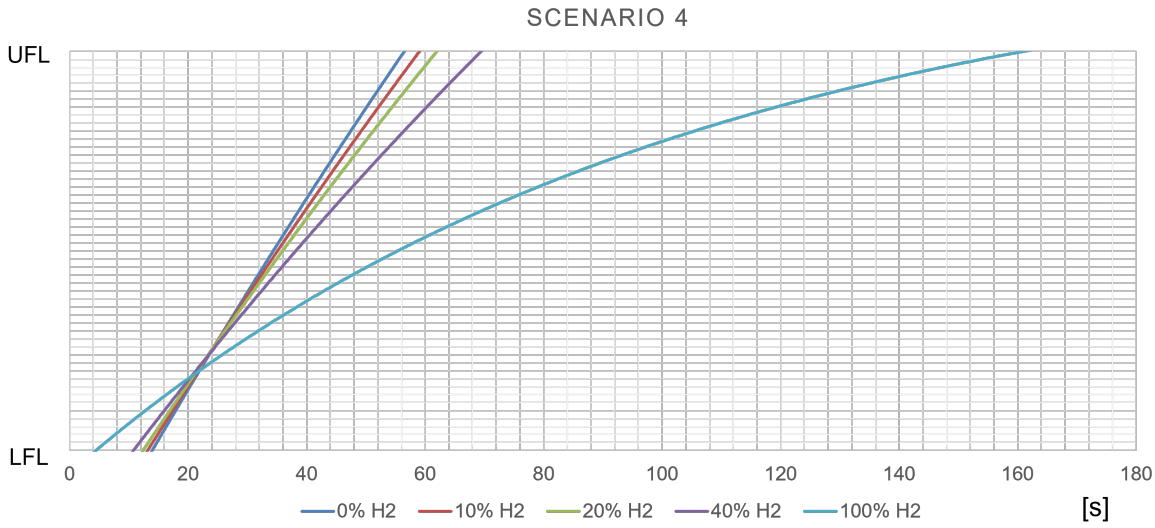

Figure 4.9: Flammability window in Scenario 4.

These charts provide a graphic representation of the concentration profiles associated with the different NGH2 mixtures for each scenario, all within their respective flammability windows, as has been previously stated, and this is fundamental in or the analysis as it provides a visual depiction of the potential fire or explosion risks at different stages.

To offer a more user-friendly comparison and an inclusive comprehension of the diverse mixture concentration profiles, the graphical data is also reported in the upcoming Table 4.4. This tabulated format aids in providing a clear and concise overview of the calculations, therefore facilitating an easier interpretation of the data's implications.

Molar H_2 %	*Scenario* 1	*Scenario* 2	*Scenario* 3	*Scenario* 4
0%	0.07 s	9 s	50 s	43 s
10%	0.07 s	9 s	55 s	46 s
20%	0.08 s	10 s	61 s	50 s
40%	0.09 s	12 s	75 s	59 s
100%	0.25 s	48 s	429 s	157 s

Table 4.4: Variance of residence time (in seconds) within the flammability window.

Taking into account the increase in conditional explosion probability, it is possible to observe the variability of the residence time in seconds within the flammability window as presented in the Table 4.4. Reviewing the data provided, it is noticeable that the variability for a blend with 10% hydrogen is approximately 10%. As a result, it is both reasonable and appropriate to conclude that there is no significant impact on the conditional probability of explosion.

4.3.2. GAME project approach

Recalling the previously introduced TNO Multi Energy model, it provides an integral component in assessing Vapour Cloud Explosions (VCEs) effects. Through a strategic combination of peak overpressure and the energy stored in the cloud, we can acquire a more detailed understanding of such explosive events (Chapter 3.2.2).

The model's importance lies in its central ability to draw a meaningful connection between an explosion's peak overpressure and the contained energy within the gas or vapour cloud. It allows for a nuanced understanding of a VCE's dynamics and potential consequences. This valuable insight contributes to more robust safety measures, efficient response strategies, and improved infrastructural designs. For more in-depth information on this topic, one might consider referring to the extensive work undertaken by Mercx, van den Berg, and van Leeuwen [45].

Looking at the provided graph that plots these values, a specific trend can be noticed. For values of the combustion energy-scaled distance (r') that are higher than 1 (as it is highlighted in Figure 4.10), curves number 6 to 10 appear to converge. This observation is crucial to our understanding and interpretation of the next steps.

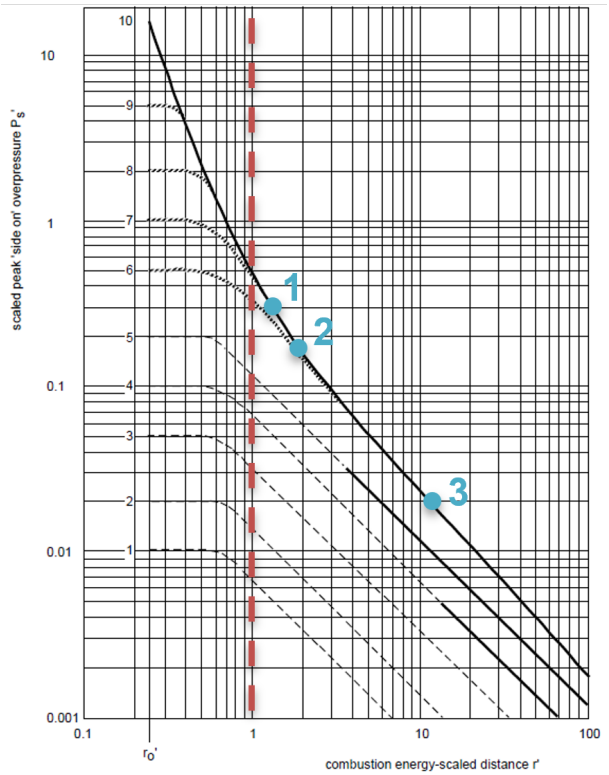

Figure 4.10

Given our objective of conducting a thorough and meticulous analysis, we adopt a conservative approach to studying the influence of the hydrogen concentration. To this end, we refer specifically and exclusively to curve 10. This particular curve, called 'blast curve', depicts the typical strength that would be associated with an explosion under these specified circumstances.

To provide further context, curves 7 to 10, as it is outlined in the Yellow Book [43], represent a blast strength category that is associated with high ignition strength, high obstruction, and confined environments. This aligns with the exact conditions that we are analyzing. Therefore, curve 10 offers an insightful and accurate representation that allows us to best understand the behavior of such an explosion.

The following three limit values have been taken into consideration Figure (4.10):

1. 300 mbar: certain mortality, failure of reinforced concrete structures.
2. 170 mbar: onset of mortality, failure of steel structures.
3. 20 mbar: reversible injuries, glass breakage.

As we continue to dig into the details of this calculation, Equation 3.31 and Equation 3.32 must be taken into account.

From the aforementioned formulas, it has been possible to derive the following equation:

$$P_{\%} = \frac{S_{L,mixture}^{2.7}}{S_{L,methane}^{2.7}} - 1 \tag{4.3}$$

This equation delineates the variations in peak pressure in relation to pure methane, due to the introduction of hydrogen into the mixture ($P_{\%}$), where S_L is laminar flame speed of the blend in cm/s. The following table displays the calculations resulting from the application of this formula across the different cases of blend composition.

$Molar\ H_2\ \%$	$Mass\ H_2\ \%$	$S_L\ [cm/s]$	$P_{\%}$
0%	0 %	37.2	0 %
10%	1.4 %	40.1	22 %
20%	3.0 %	43.9	56 %
40%	7.7 %	54.4	179 %
100%	100 %	285	24313 %

Table 4.5

From the performed calculations shown in Table 4.5, it can be observed that with an increasing concentration of hydrogen, the expected peak pressure increases, assuming constant geometrical characteristics of the congested area. This trend underscores the significance of the hydrogen concentration in the mixture and the potential amplification of the peak pressure under certain conditions.

As the analysis progresses, it becomes necessary to calculate the explosion radius corresponding to the previously mentioned overpressure cases, for all various oxygen concentrations considered in the NGH2 mixture. However, before proceeding with these calculations, the values of Higher Heating Value (HHV) for the different compositions must be computed and discussed. A comprehensive understanding of these values is crucial for the accurate determination of the explosion radius and the subsequent assessment of associated risks.

	$HHV\ [MJ/kg]$	$LHV\ [MJ/kg]$
Hydrogen	141.8	121
Methane	55.5	50

Table 4.6: HHV and LHV values for pure hydrogen and pure methane [20].

The HHV values for every studied blend composition have been calculated using the following formula, being X_{H2} the mass composition of hydrogen in the mixture and ρ_{mix} the density of the mixture in kg/m^3 for every studied case (Table 4.7).

$$HHV_{mix,mass} = X_{H2} * HHV_{H2} + (1 - X_{H2}) * HHV_{CH4} \qquad [MJ/kg] \qquad (4.4)$$

$$HHV_{mix,vol} = HHV_{mix,mass} * \rho_{mix} \qquad [MJ/m^3] \qquad (4.5)$$

$Molar\ H_2\ \%$	$Mass\ H_2\ \%$	$HHV_{mix}\ [MJ/kg]$	$\rho_{mix}\ [kg/m^3]$	$HHV_{mix}\ [MJ/m^3]$
0%	0 %	55.5	0.66	37
10%	1.4 %	56.7	0.60	34
20%	3.0 %	58.1	0.54	32
40%	7.7 %	62.2	0.43	27
100%	100 %	141.8	0.08	12

Table 4.7

As showed in Table 4.7, it can be observed that with an increasing percentage of hydrogen in the mixture, the higher heating values (HHV) per mass unit slightly rise. This rise can be attributed to the inherently high energy content of hydrogen when compared to natural gas. Nevertheless, given the fact that the density of the mixture concurrently decreases with the increase in hydrogen content, there is an inverse effect on the HHV when expressed on a volumetric basis, which is of significant relevance for this analysis.

Now, contemplating the previously mentioned reference overpressure values (failure of reinforced concrete structures, failure of steel structures, and glass breakage), it is possible, by observing the progression of Curve 10, to derive the corresponding r' values for these three cases. These values are systematically tabulated in Table 4.8. Through this data, one can make a fair comparison between the different cases and further understand the implications in the various scenarios.

	P'_s	r'
Failure of reinforced concrete structures	0.3	1.35
Failure of steel structures	0.17	1.9
Glass breakage	0.02	11.6

Table 4.8

Utilizing the previously derived values, it is now feasible, using Equation 3.32, to determine the explosion radius for each aforementioned case. This calculation is executed by considering the corresponding total combustion energies for each considered scenario and blend composition, as it is shown in Table 4.9.

Scenario	*Molar* H_2 %	Distance [m] @300 mbar	Distance [m] @170 mbar	Distance [m] @20 mbar
Scenario 2	0 %	15	21	129
	10 %	15	21	126
	20 %	14	20	123
	40 %	14	19	116
	100 %	10	15	89
Scenario 3	0 %	65	92	561
	10 %	64	90	548
	20 %	62	87	534
	40 %	59	83	504
	100 %	45	63	384
Scenario 4	0 %	26	37	227
	10 %	26	36	222
	20 %	25	35	216
	40 %	24	33	204
	100 %	18	25	155

Table 4.9

When examining Table 4.9, it becomes evident that the calculated radii of overpressure decrease in the various scenarios as the amount of hydrogen in the mixture increases. The interpretation of these findings leads to a key insight: the impact on the distances reached by dangerous overpressure values in the event of VCEs does not undergo a significant

alteration. Thus, these variations can be considered negligible. This indicates that there is no compelling necessity for the introduction of additional procedures beyond those already in practice in natural gas (NG) facilities. The adoption of NG facilities' standard operational procedures appears to suffice in addressing the risks and consequences related to the variations in the hydrogen concentration within the mixtures.

Therefore, while it is essential to continue safety assessments and monitoring, the current safety strategies appear to hold their effectiveness even with the increased presence of hydrogen.

4.4. CFD Simulations

Progressing further in the discourse, it is paramount to bring attention to the remarkable utility of Computational Fluid Dynamics (CFD) simulations. These simulations served as an indispensable tool in conducting a proper analysis of the behaviour exhibited by the NGH2 gas mixture cloud. The variability in the behaviour of this cloud will be thus examined, with particular emphasis placed on observing how the behaviour of the said cloud changes using the different hydrogen concentrations in the blend.

To fit the specific requirements of scenarios 2, 3, and 4, several parameters were systematically adjusted. These scenarios, it is worth mentioning, are grounded in realistic geometric configurations (recreated with ANSYS® SpaceClaim). The use of these carefully simulated environments is a key point in enhancing the practicality and relevance of the investigation.

A structured set of well thought-out considerations was employed to obtain a robust and accurate comparison with the analytically proposed data. It is through this process that the multi-layered complexity and precision of the study are underlined. In conclusion, with the creation a bridge between the theoretical explorations and the tangible real-world scenarios, the work takes a step forward towards delivering well-informed, effective, and future-oriented solutions.

4.4.1. Birch's Equivalent Diameter

Referring to Chapter 3.1.8, it is of utmost importance to consider the computation of an equivalent diameter before proceeding with further calculations. This equivalent diameter can be calculated using Birch's approach, as outlined in Formula 3.30. The results of the equivalent diameter calculations, which have been conducted across the various scenarios, can be found in Table 4.10.

Scenario	*Molar* H_2 %	*Equivalent Diameter* $[m]$
Scenario 2	0 %	0.04707
	10 %	0.04707
	20 %	0.04706
	40 %	0.04706
	100 %	0.04681
Scenario 3	0 %	0.01215
	10 %	0.01215
	20 %	0.01215
	40 %	0.01215
	100 %	0.01209
Scenario 4	0 %	0.03843
	10 %	0.03843
	20 %	0.03843
	40 %	0.03842
	100 %	0.03821

Table 4.10: Equivalent diameters set calculated using Birch's approach

4.4.2. Mesh

The development of an appropriate mesh is fundamentally crucial in CFD calculations to ensure accurate and reliable results. Given this, it was decided to employ parameters that would best align with the context of the study. Specifically, a progressive volumetric growth pattern (less than or equal to 1.2) was adopted, starting from a millimetric cell size in proximity to the release nozzle.

The user-friendly functionalities of the ANSYS® Fluent Meshing has been used to create a mesh that would be suitable for the calculation context. The local sizing parameters

were instrumental in gaining better control over the mesh size distribution, and in defining specific mesh size controls that operate on specific, localized portions of the geometry and mesh.

By choosing a Target Mesh size of one millimeter and a Growth Rate of 1.2, it was possible to create an appropriate cell density around the release point, which then progressively decreased as it moved away from that point.

Subsequently, regarding the Surface Mesh parameters, it was decided to consistently use the value of 1 mm as the Minimum Size and about 3 m (depending on the case) as the Maximum Size, while the Growth Rate parameter maintained a value of 1.2.

Following this, a boundary layer was created to ensure a smoother transition of the mesh, using the standard parameters proposed by the software.

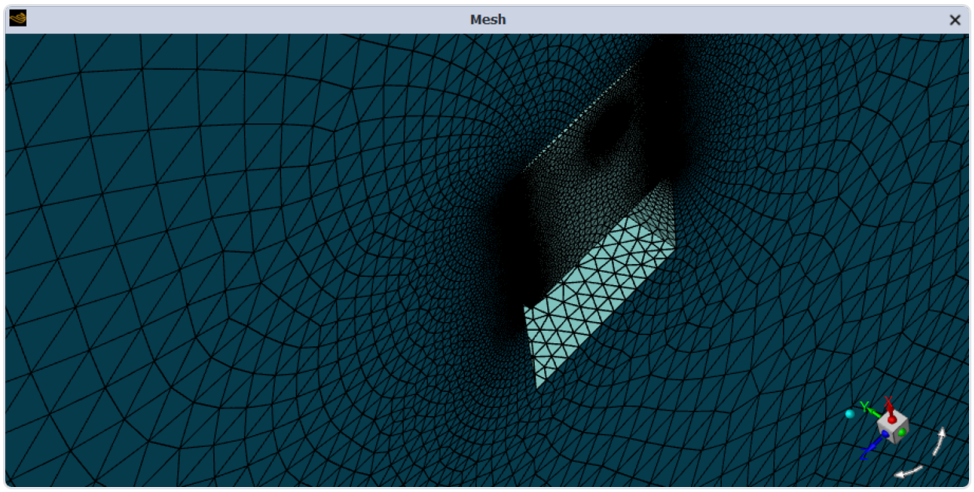

Figure 4.11: Detail of Scenario 3 mesh.

Finally, for what concerns the Volume Mesh parameters, it was decided to use tetrahedral-shaped cells, given the relatively complex nature of the geometries, and to consistently use a Growth Rate of 1.2 or slightly less (for higher density). This comprehensive approach to mesh development was fundamental in ensuring the accuracy and reliability of the calculations.

4.4.3. ANSYS® Fluent Setup

For the composition of the fluid within the computational domain, the default "air species" provided by Fluent was selected. ANSYS® Fluent offers a variety of Equation of State (EoS) models, including the Incompressible Ideal Gas Law, Ideal Gas Law for Compressible Flow, Volume Weighted Mixing Law, Redlich-Kwong-Soave (RKS), Redlich-Kwong (RK), and Peng-Robinson (PG). Among these available models, the decision was made to primarily focus on the first one, the Incompressible Ideal Gas Law.

As for the wind conditions, a speed of 5 m/s was used. For the third scenario, three different wind directions from three different angles were considered, as can be seen in Figure 4.12. This approach was taken to align with the model mentioned in Chapter 4.2. The consideration of varying wind directions adds a layer of complexity and realism to the simulations, allowing for a more comprehensive understanding of the system under different environmental conditions.

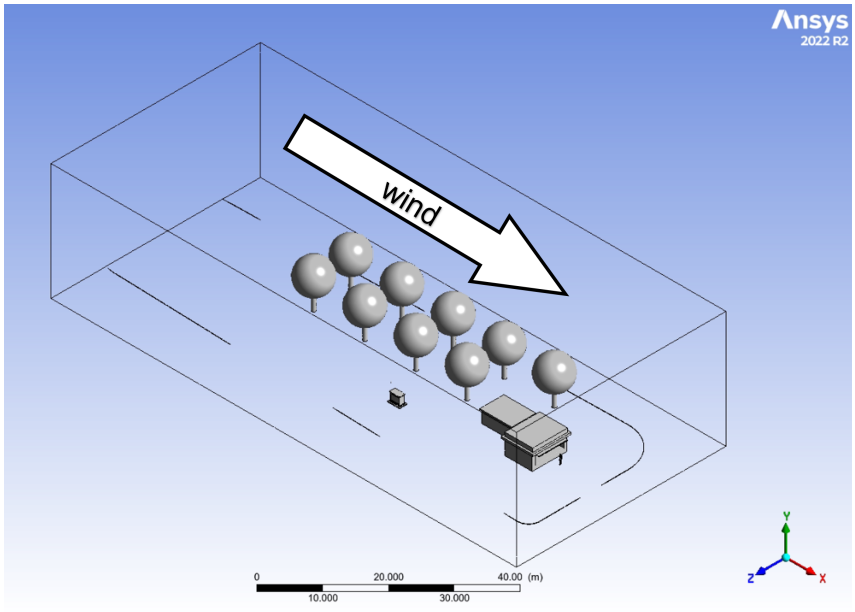

Figure 4.12: Representation of the wind direction in Scenario 2.

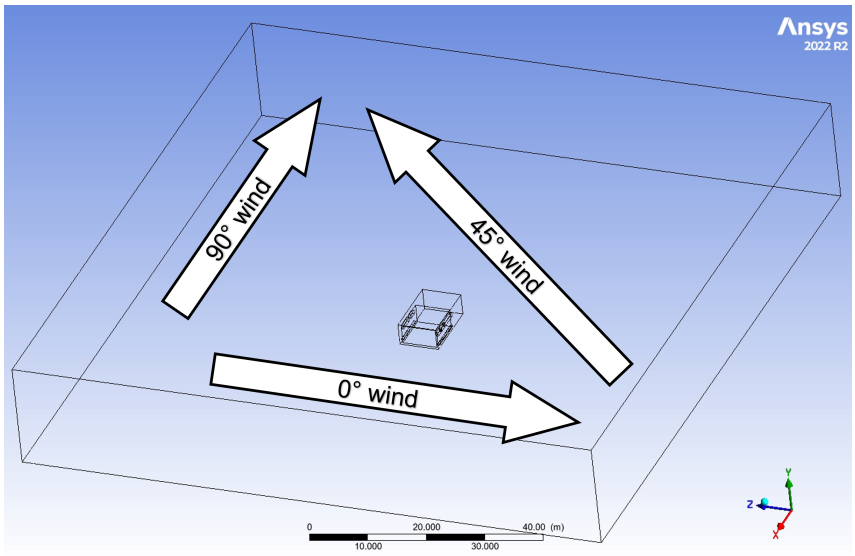

Figure 4.13: Representation of the chosen wind directions for Scenario 3.

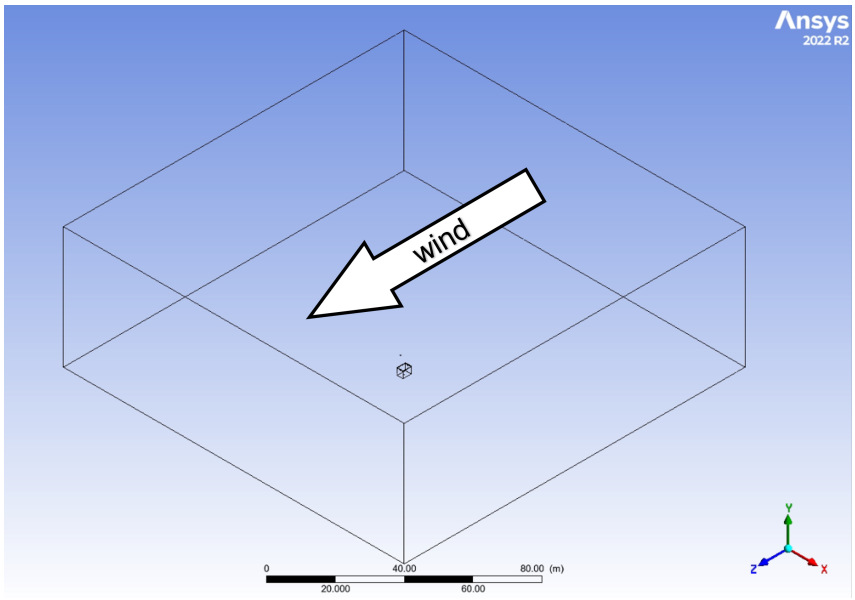

Figure 4.14: Representation of the wind direction in Scenario 4.

For what concerns the walls, the decision was made to use the walls provided standard parameters in Fluent. However, for the surfaces that constitute the enclosure containing the geometry, it was determined that they should be considered as free-slip walls. This approach allows for a more realistic simulation of the fluid dynamics within the enclosure, as it takes into account the lack of friction or shear stress on these surfaces.

The solution was obtained by configuring the ANSYS® Fluent calculation software to define the conditions for solving the equations and setting the boundary conditions for

each surface. The simulations were all conducted under steady-state conditions, utilizing a pressure-based solver type. The settings for these simulations are detailed in Table 4.11. While most settings remained constant across each simulation, there were exceptions. These included the NGH2 mass flow rate and the composition of the considered blend, always using the aforementioned different options.

Solution Method	*Scheme*
Pressure-velocity coupling	Coupled – pseudo transient
Spatial discretisation	*Scheme*
Gradient	Least square cell based
Pressure	Second order
Density	Second order upwind
Momentum	Second order upwind
Turbulent kinetic energy	Second order upwind
Energy	Second order upwind
Specific dissipation rate	Second order upwind
Other settings	
Gravity	-9.81 m/s2 along y-direction
Iterations	Until convergence criteria is reached
Initialisation scheme	Hybrid

Table 4.11: ANSYS® Fluent settings.

Regarding the convergence criterion, the default setting provided by the solver was employed. This setting is based on the attainment of standard values that pertain to the scaled residual equations. In the realm of fluid dynamics, these standard values are generally accepted as sufficient for achieving convergence in most problems. Specifically, a value on the order of magnitude of 10^{-6} for energy and 10^{-3} for all other equations is typically considered adequate [4]. This approach ensures that the solution reached is stable and reliable, providing a solid foundation for the analysis and interpretation of the simulation results. It's worth noting that these values are not arbitrary but have been established through extensive experience and consensus within the fluid dynamics community. They serve as a benchmark for determining when a solution is sufficiently accurate for practical purposes.

4.4.4. Results

In order to properly analyze the results obtained from the CFD simulations and compare them with the results gained with PHAST, a specific and meaningful indicator was chosen. The decision was made to measure the downwind distance and the ground clearance of the plume of the NGH2 mixture cloud at the concentration corresponding to the Lower Flammability Limit (LFL).

These parameters serve as a tangible index to show how, unlike similar data derived from the PHAST software (Table 4.13), the confinement of the release in a realistic situation is taken into consideration in a proper CFD simulation. This includes considerations of a realistically plausible geometry, the effect of turbulence in specific scenarios, and the overall environment. By focusing on this particular parameter, we can gain a more nuanced understanding of the behavior of the NGH2 mixture cloud under different conditions. This approach allows for a more comprehensive and accurate comparison between the CFD simulations and the given data, thus enhancing the overall quality and reliability of the analysis.

Scenario	*Molar* H_2 %	Downwind distance [m]	Ground clearance [m]
Scenario 2	0 %	4	2
	10 %	4	2
	20 %	4	4
	40 %	4	2
	100 %	5	2
Scenario 3	0 %	15	2
	10 %	15	3
	20 %	15	3
	40 %	14	3
	100 %	15	5
Scenario 4	0 %	4	1
	10 %	4	1
	20 %	4	1
	40 %	4	1
	100 %	5	1

Table 4.12: Plume parameters provided by PHAST.

For what concerns the CFD simulations, the following derived data echoes the anticipated outcomes for the various NGH2 blends with different compositions of hydrogen. Indeed, as can be observed from Table **4.13**, the data differs significantly from the previously provided calculations completed with PHAST (Table 4.13). Some assumptions have been made for the comparison, based on the measures taken.

Notably, the calculation of the plume height from the ground is a directly comparable data point, with the ground acting as the reference point. However, for the downwind distance of the plume, several reference points have been used across various geometries to make the data properly comparable. More specifically, for Scenario 2, the measurement was taken from the farthest end of the cabin openings under consideration. In scenario 4, on the other hand, the measurement was taken from the downwind end of the highest ventilation opening. Lastly, for scenario 3, two different criteria were adopted: for wind directions of 0° and 45°, the distance was measured perpendicularly from the downwind window; whereas for the case with a wind direction of 90°, a similar approach to scenario 2 was chosen, considering the distance from the farthest end point in relation to the wind direction.

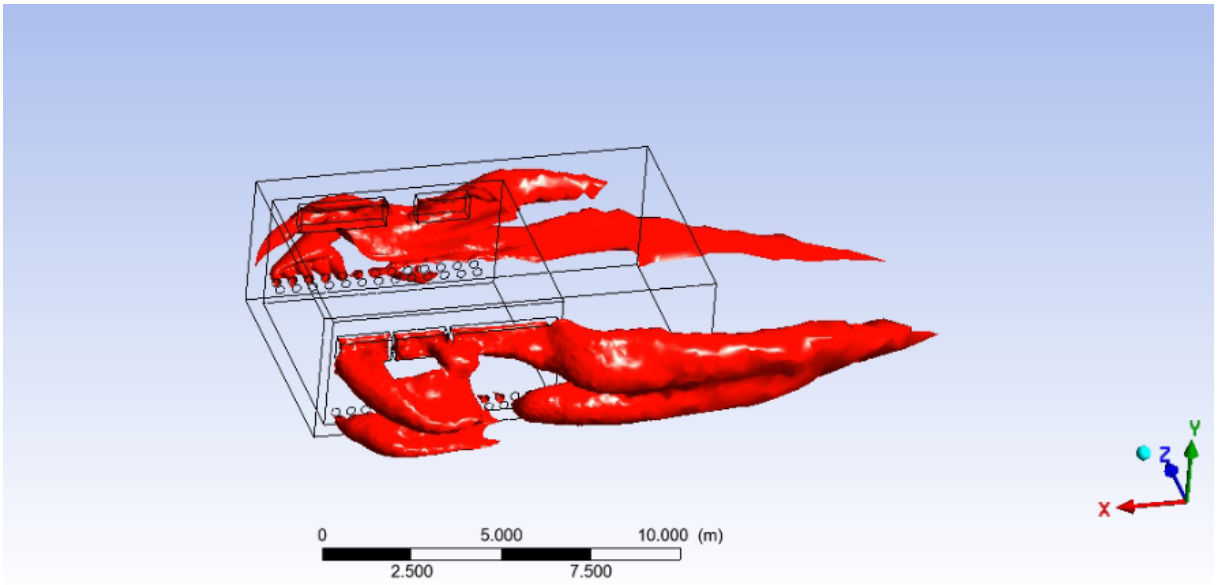

Figure 4.15: Scenario 3: LFL isosurface of pure hydrogen (90° wind).

In relation to the obtained data, a resemblance is observed in the behaviour of the limit cases where a release of pure methane or pure hydrogen is anticipated. Indeed, hydrogen, being significantly lighter, tends to result in a considerably higher plume upon its release compared to methane. Regarding the intermediate cases, however, the considered mixtures tend to exhibit a behaviour strikingly similar to that of pure methane, regardless

of the scenario. This observation is highly critical for the development and future of this application as the flammability zone's conformation displays negligible differences in all the considered applications. This finding could be the foundation for conducting more in-depth studies but already outlines the success and effectiveness of this analysis.

In conclusion, the differences between the PHAST-provided data and the data calculated with Fluent's CFD simulations mainly stem from the fact that the containment of the releases tends to favour highly accentuated turbulence phenomena within, thoroughly mixing the NGH2 mixture. Meanwhile, the interaction with the wind flow outside the structures, obviously aerodynamically altered by the considered structures, tends to significantly dampen the development of zones with a risk of flammability. This consequence is critically important for preserving the surrounding environment and risk assessment in the study of future similar scenarios.

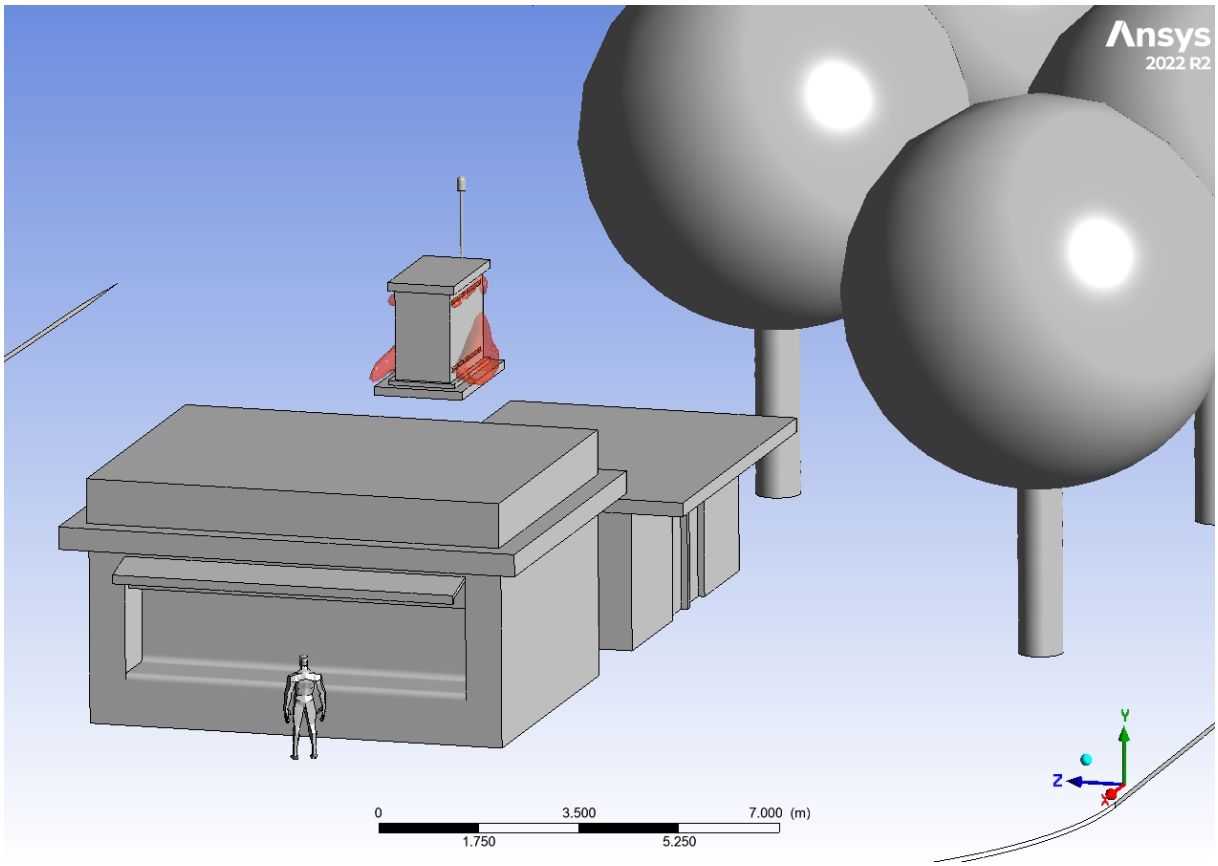

Figure 4.16: Scenario 2: LFL isosurface of pure methane.

Scenario	*Molar H_2 %*	Downwind distance [m]	Ground clearance [m]
Scenario 2	0 %	0.49	1.90
	10 %	0.45	2.00
	20 %	0.43	1.89
	40 %	0.41	2.06
	100 %	1.67	2.36
Scenario 3 (0° wind)	0 %	1.07	2.93
	10 %	2.42	3.25
	20 %	2.72	3.12
	40 %	3.40	3.90
	100 %	6.73	5.51
Scenario 3 (45° wind)	0 %	3.64	3.32
	10 %	2.97	3.01
	20 %	2.65	3.54
	40 %	2.59	3.43
	100 %	6.44	3.71
Scenario 3 (90° wind)	0 %	0.05	2.93
	10 %	0.44	2.93
	20 %	0.53	2.93
	40 %	1.17	2.93
	100 %	11.35	3.04
Scenario 4	0 %	8.61	8.963
	10 %	8.62	8.91
	20 %	8.00	9.65
	40 %	9.30	9.23
	100 %	10.42	15.69

Table 4.13: Plume parameters calculated with ANSYS® Fluent.

5 | Mesh Sensitivity Analysis

A mesh sensitivity analysis is a critical component in a CFD work. This analysis is performed by running simulations using grids of varying resolutions, with some grids being up to many times denser in cells than the initial grid. The primary purpose of this analysis is to investigate the degree of variation in the converged solution with each change in the mesh.

In essence, a mesh sensitivity analysis is a systematic approach to understanding how changes in the mesh, or the grid used in the simulation, affect the final results. This is crucial because the accuracy and reliability of CFD simulations are heavily dependent on the quality and resolution of the mesh used. A mesh that is too coarse may not capture the necessary details of the fluid flow, while a mesh that is too fine may require excessive computational resources. Therefore, finding the right balance is key, and this is where a mesh sensitivity analysis comes into play.

In the context of this specific study, Scenario 1 is selected for the analysis, with the wind direction kept constant at 0°, using the fixed concentration of 20% for the NGH2 blend released, and an arbitrary fixed value of methane mass concentration of 0.004. By maintaining the same scenario and settings, the focus was solely on the precision of the mesh as its resolution is increased or decreased. This approach ensures that any changes observed in the results can be attributed to the changes in the mesh, rather than other variables.

The behavior of the mesh is analyzed by automatically increasing the Volume Mesh Growth Rate in ANSYS® Fluent meshing, which results in denser meshes. This adjustment leads to the creation of five different meshes, each with an increasing number of cells: one with 2.1 million cells (the one used for all the previous calculations), one with 3.1 million, one with 4.0 million, one with 8 million, and one with 11 million.

The accuracy of the calculations for these different mesh resolutions is then verified using a spatial parameter. Specifically, the distance between the downwind window and the furthest point reached by the vapor cloud in the wind direction is chosen as the parameter. This parameter is a practical measure that can provide insights into the dispersion of the

vapor cloud, which is a critical aspect of the study.

The results of the mesh sensitivity analysis are presented in the following plots. Upon examination, it is found that there are no discernible trends in the result data. This means that the changes in the mesh do not lead to significant changes in the results, indicating that the mesh resolutions used are appropriate for the purpose of this study. The differences observed in the various findings are within acceptable limits, suggesting that the results are robust and reliable. This conclusion underscores the importance of conducting a mesh sensitivity analysis in CFD work, as it provides confidence in the validity of the results.

From this analysis, it becomes evident that the validity of these calculations is not confined to this specific scenario alone. Instead, it can be extrapolated and applied to all other cases of computational fluid dynamics (CFD) simulations that have been explored in this study. This broad applicability is a significant finding, as it underscores the robustness and reliability of the methods used. This conclusion is reached by taking into account the extreme proximity of the parameter values that were employed in the creation of the various meshes. The consistency in these values across different meshes suggests that the results are not overly sensitive to minor changes in the mesh parameters. Therefore, even as the mesh resolution is increased or decreased, the core findings remain stable and reliable.

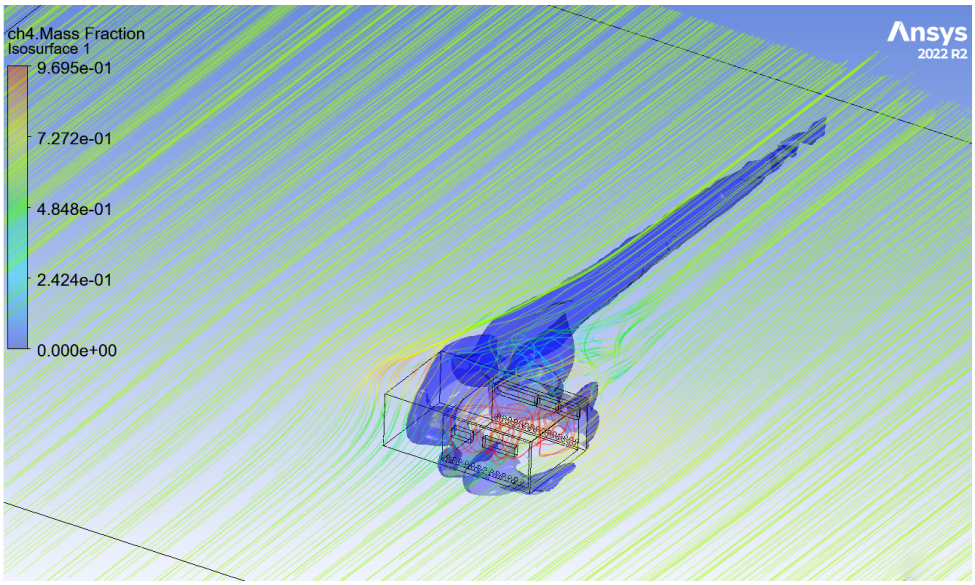

Figure 5.1: 0.004 methane mass fraction isosurface surrounded by velocity streamlines.

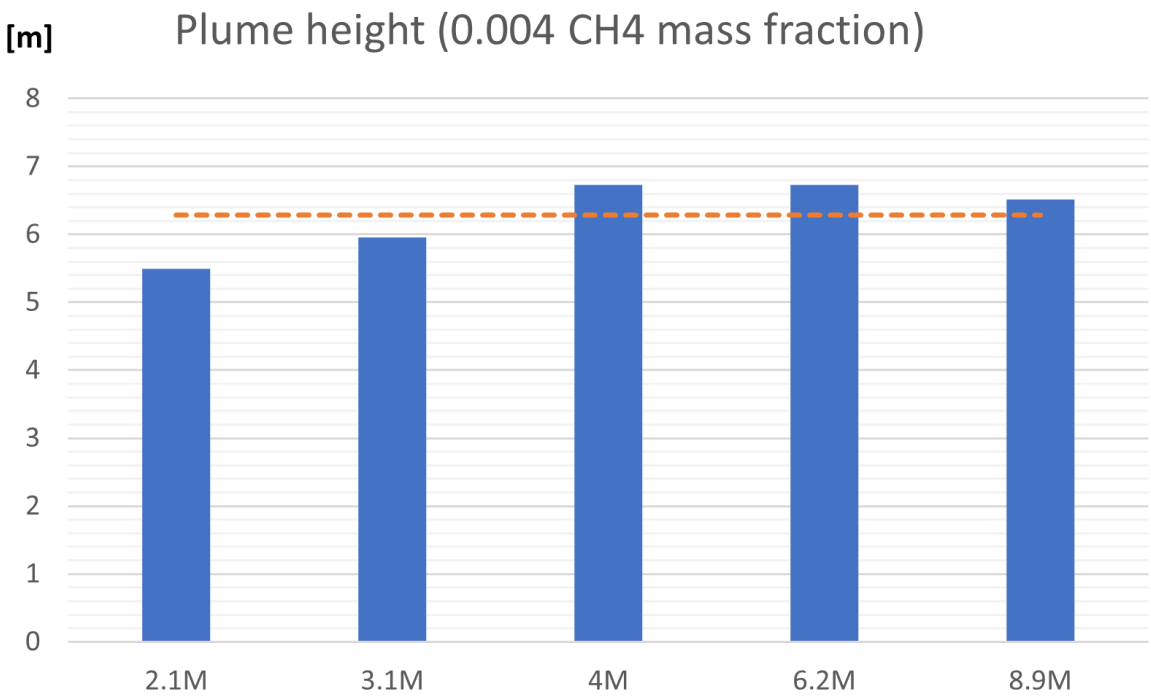

Figure 5.2: Plume height results for the mesh sensitivity analysis.

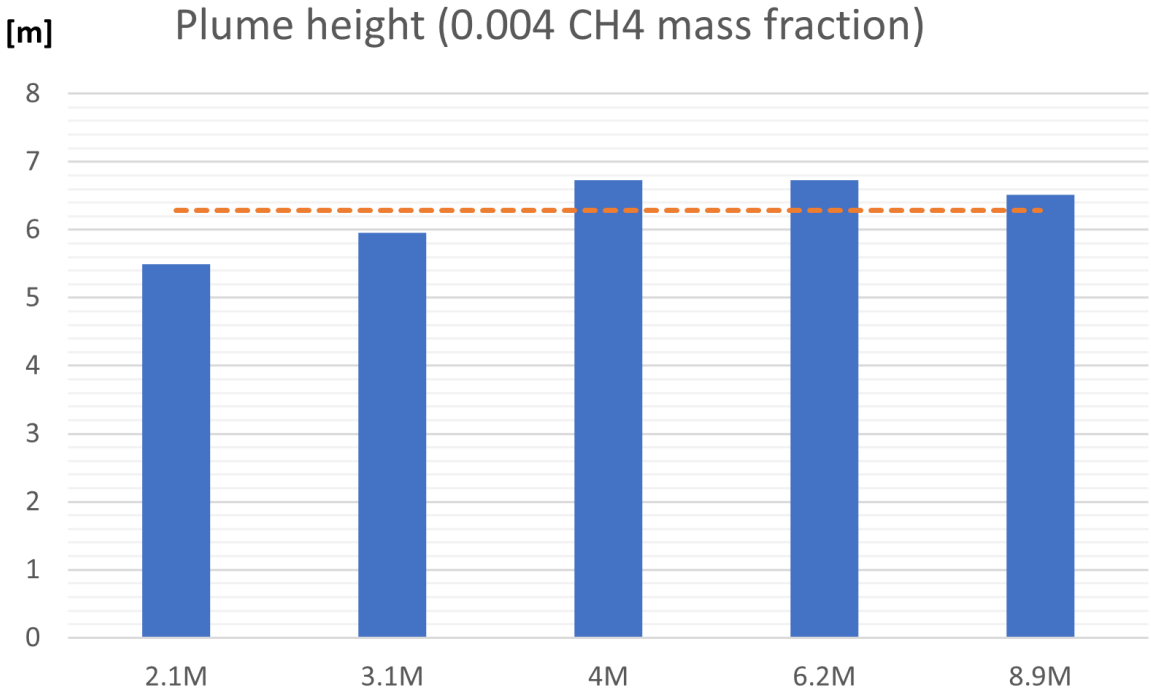

Figure 5.3: Plume length results for the mesh sensitivity analysis.

6 | Conclusions

- This thesis work has provided a comprehensive examination of the dynamics and potential consequences of VCEs, with a particular focus on the behaviour of various representative blends of NGH2. The meticulous analysis conducted throughout the study has yielded valuable insights that can contribute to the development of more robust safety measures, efficient response strategies, and improved infrastructural designs.
- The findings of this study underscore the importance of a detailed understanding of hydrogen combustion in the context of VCEs. The insights gained from the analysis can significantly contribute to the development of safety measures and infrastructural designs that can mitigate the risks associated with hydrogen combustion. The study has also highlighted the importance of considering the total combustion energies for each scenario and blend composition. The derived values have enabled the determination of the explosion radius for each case, providing a fair comparison between the different cases and further understanding the implications in the various scenarios.
- In line with the specifications detailed in CEI EN 60079-10-1, which states, "With gas mixtures, the gas group should be considered as IIC or IIB+H2 where a gas mixture includes 30% or more of hydrogen by volume", it's crucial to note the implications this carries for the management of infrastructure and safety protocols in relevant industries. Moreover, there is no need for different procedures or personal protective equipment (PPE) compared to those already in use for managing natural gas (NG) facilities. Furthermore, current detectors do not pose a risk of ignition for the flammable mixture. If the specifications of the detectors do not indicate "suitable for H2", it might be beneficial to re-evaluate the activation threshold to account for the lower quantity of NG.
- Notably, the findings have made a significant contribution to the understanding of the behaviours of different fluid mixtures, revealing nuances that hold implications for a range of applications. The insight that hydrogen and methane, despite their

individual characteristics, exhibit similar behaviours in certain contexts is particularly noteworthy. This understanding lays a solid groundwork for the advancement of this area of study.

- Furthermore, the nuanced understanding of flammability zones uncovered through this research holds considerable promise for real-world application, impacting safety measures, risk assessments, and the design of future scenarios. The fact that these zones present negligible variations across different scenarios underlines the reliability of the CFD simulations and their potential utility in a broader context.
- The successful results of this study have implications that reach far beyond its immediate context. They endorse the effectiveness of CFD as a tool for complex fluid dynamics analysis, demonstrating its capacity for generating reliable, reproducible, and insightful data.
- this research humbly adds a layer of understanding to the expansive field of Computational Fluid Dynamics. The favourable outcomes from the simulations reinforce the chosen methodology, while also nurturing a sense of optimism for what lies ahead. It is hoped that the outcomes will act as encouragement for the enduring use of CFD simulations in shedding light on increasingly intricate phenomena.
- Significant findings from this research underscore the potential role of hydrogen as a sustainable energy vector. The nuances revealed by the simulations illuminate how hydrogen behaves under varied conditions, providing insights that may be vital for its efficient and safe utilization in real-world scenarios. In the broader context of environmental sustainability and energy security, the potential implications of this research are profound. Understanding the behaviors of hydrogen not only aids in its efficient exploitation but also contributes to our capacity to mitigate environmental challenges.

Bibliography

[1] B. Angers, A. Hourri, P. Bénard, and A. V. Tchouvelev. Numerical investigation of a vertical surface on the flammable extent of hydrogen and methane vertical jets. 2011.

[2] P. Bénard, A. Hourri, B. Angers, A. V. Tchouvelev, and V. Agranat. Effects of surface on the flammable extent of hydrogen jets. 2009.

[3] P. Bénard, A. Hourri, B. Angers, and A. Tchouvelev. Adjacent surface effect on the flammable cloud of hydrogen and methane jets: Numerical investigation and engineering correlations. *International Journal of Hydrogen Energy*, 41(41):18654–18662, 2016.

[4] A. Birch, D. Brown, M. Dodson, and F. Swaffield. The structure and concentration decay of high pressure jets of natural gas. *Combustion Science and technology*, 36 (5-6):249–261, 1984.

[5] L. C.D. What causes unconfined vapour cloud explosions? *Loss Prevention*, 9: 101–105, 1975.

[6] C. J. Chen and W. Rodi. Vertical turbulent buoyant jets: a review of experimental data. *NASA Sti/Recon Technical Report A*, 80:23073, 1980.

[7] M. Derudi, D. Bovolenta, V. Busini, and R. Rota. Heavy gas dispersion in presence of large obstacles: selection of modeling tools. *Industrial & Engineering Chemistry Research*, 53(22):9303–9310, 2014.

[8] M.-L. Ducasse, J. Dubois, M. Amielh, and F. Anselmet. Experimental investigation of a turbulent variable density jet impinging on a sphere. In *Proceedings of the 15th international symposium on applications of laser techniques to fluid mechanics, Lisbon*, 2010.

[9] A. Ennis. Development of source terms for gas dispersion and vapour cloud explosion modelling. In *Institution of Chemical Engineers Symposium Series*, volume 151, page 108. Institution of Chemical Engineers; 1999, 2006.

[10] A. Fluent. Ansys fluent theory guide 15.0. *ANSYS, Canonsburg, PA*, 33, 2013.

[11] E. Franquet, V. Perrier, S. Gibout, and P. Bruel. Free underexpanded jets in a quiescent medium: A review. *Progress in Aerospace Sciences*, 77:25–53, 2015.

[12] E. H. Gefaehrdungspotential bei einem verstaerkten Wasserstoffeinsatz. Deutsche Forschungsanstalt fuer Luft- und Raumfahrt (DLR), Stuttgart, Germany, 1992.

[13] J. E. Hall, P. Hooker, L. O'Sullivan, B. Angers, A. Hourri, and P. Bernard. Flammability profiles associated with high-pressure hydrogen jets released in close proximity to surfaces. *international journal of hydrogen energy*, 42(11):7413–7421, 2017.

[14] N. S. Holmes and L. Morawska. A review of dispersion modelling and its application to the dispersion of particles: an overview of different dispersion models available. *Atmospheric environment*, 40(30):5902–5928, 2006.

[15] A. Hourri, B. Angers, P. Bénard, A. Tchouvelev, and V. Agranat. Numerical investigation of the flammable extent of semi-confined hydrogen and methane jets. *international journal of hydrogen energy*, 36(3):2567–2572, 2011.

[16] A. D. L. Inc. Final report on an investigation of hazards associated with the storage and handling of liquid hydrogen. Technical Report C-61092, Arthur D. Little Inc., Cambridge, USA, 1960. Report still classified.

[17] H.-S. Kang, S.-M. Kim, and J. Kim. Safety issues of a hydrogen refueling station and a prediction for an overpressure reduction by a barrier using openfoam software for an sri explosion test in an open space. *Energies*, 15(20), 2022. ISSN 1996-1073. doi: 10.3390/en15207556. URL `https://www.mdpi.com/1996-1073/15/20/7556`.

[18] S. Kim and Y. Kim. Review: Hydrogen tank explosion in gangneung, south korea. In *Cent. Hydrog. Saf. Conf*, 2019.

[19] J. G. Koomey, S. Berard, M. Sanchez, and H. Wong. Web extra appendix: implications of historical trends in the electrical efficiency of computing. *IEEE Annals of the History of Computing*, 33(3):S1–S30, 2011.

[20] P. Linstorm. Nist chemistry webbook, nist standard reference database number 69. *J. Phys. Chem. Ref. Data, Monograph*, 9:1–1951, 1998.

[21] S. Liu, C. Meneveau, and J. Katz. On the properties of similarity subgrid-scale models as deduced from measurements in a turbulent jet. *Journal of Fluid Mechanics*, 275: 83–119, 1994.

[22] M. LLC. Biennial report on hydrogen safety, 2011. URL `http://www.hysafe.net/wiki/BRHS/OFD-Chapter1`.

[23] U. Manual. Ansys fluent 12.0. *Theory Guide*, 2009.

[24] A. MARTANI. Vertical cylindrical tank influence on high-pressure jets: a computational fluid dynamic study. 2019.

[25] A. Mazzoldi, T. Hill, and J. J. Colls. Cfd and gaussian atmospheric dispersion models: A comparison for leak from carbon dioxide transportation and storage facilities. *Atmospheric environment*, 42(34):8046–8054, 2008.

[26] F. R. Menter. Two-equation eddy-viscosity turbulence models for engineering applications. *AIAA journal*, 32(8):1598–1605, 1994.

[27] Z. M.G. *Safety with cryogenic fluids*. Plenum Press, New York, 1967.

[28] M. Pontiggia, V. Busini, M. Ronzoni, G. Uguccioni, R. Rota, et al. Effect of large obstacles on high momentum jets dispersion. *Chemical Engineering Transactions*, pages 523–528, 2014.

[29] P.Salcher and J.Whitehead. Uber den aus uss stark verdichteter luft. sitzungsber,. *Akademie d. Wissenschaften Wien*, 1889.

[30] L. Ragozzino. Methane high pressure jets ground interaction cfd analysis for safety purpose applications. 2017.

[31] P. Richards and R. Hoxey. Appropriate boundary conditions for computational wind engineering models using the k-ϵ turbulence model. *Journal of wind engineering and industrial aerodynamics*, 46:145–153, 1993.

[32] F. Rigas and P. Amyotte. *Hydrogen safety*. CRC Press, 2012.

[33] F. Rigas and P. Amyotte. Myths and facts about hydrogen hazards. In *13th International Symposium on Loss Prevention and Safety Promotion in the Process Industries, Florence, Italy (May 12-15, 2013)*, 2013.

[34] F. Rigas and S. Sklavounos. Hydrogen safety. In *Hydrogen Fuel*, pages 547–580. CRC Press, 2008.

[35] R. Rota. Modellazione delle conseguenze di incidenti industriali.

[36] R. Schefer, W. Houf, T. Williams, B. Bourne, and J. Colton. Characterization of high-pressure, underexpanded hydrogen-jet flames. *International journal of hydrogen energy*, 32(12):2081–2093, 2007.

[37] U. Schumann, H. Schlager, F. Arnold, R. Baumann, P. Haschberger, and O. Klemm. Dilution of aircraft exhaust plumes at cruise altitudes. *Atmospheric Environment*, 32(18):3097–3103, 1998.

[38] T.-H. Shih, W. W. Liou, A. Shabbir, Z. Yang, and J. Zhu. A new k-ϵ eddy viscosity model for high reynolds number turbulent flows. *Computers & fluids*, 24(3):227–238, 1995.

[39] C. F. Sposato, W. Rogers, and M. Mannan. Effects of obstacle geometry on jet mixing for releases of silane. In *Mary K O'Connor Process Safety Symposium. Proceedings 2000.* Mary Kay O'Connor Process Safety Center, 2000.

[40] T. S.R., S. M.P., B. W.B., S. J.E., K. R., and L. J.H.S. Detonation cell size measurements in hydrogen-air-steam mixtures. *Progress in Astronautics Aeronautics*, 106: 205–219, 1986.

[41] W. Szablewski. Be launder and db spalding, mathematical models of turbulence. 169 s. m. abb. london/new york 1972. academic press. preis geb. *Zeitschrift Angewandte Mathematik und Mechanik*, 53(6):424–424, 1973.

[42] W. THAYER III and R. Corlett. Gas dynamic and transport phenomena in the two-dimensional jet interaction flowfield. *AIAA Journal*, 10(4):488–493, 1972.

[43] C. Van den Bosch and R. Weterings. Yellow book—methods for the calculation of physical effects due to releases of hazardous materials (liquids and gases). *Committee for the Prevention of Disasters, Tech. Rep. CPR E*, 14:1997, 1997.

[44] H. K. Versteeg and W. Malalasekera. *An introduction to computational fluid dynamics: the finite volume method.* Pearson education, 2007.

[45] W. Werex, A. Van den Berg, and D. van Leeuven. Application of correlations to quantify the source strength of vapour cloud explosions in realistic situations, final report for the project:'games'. *TNO report PML*, page C53, 1998.

[46] D. C. Wilcox et al. *Turbulence modeling for CFD*, volume 2. DCW industries La Canada, CA, 1998.

[47] A. Yule. Large-scale structure in the mixing layer of a round jet. *Journal of Fluid Mechanics*, 89(3):413–432, 1978.

A | Appendix A: 3D model dimensioning of scenarios

A.1. Scenario 2

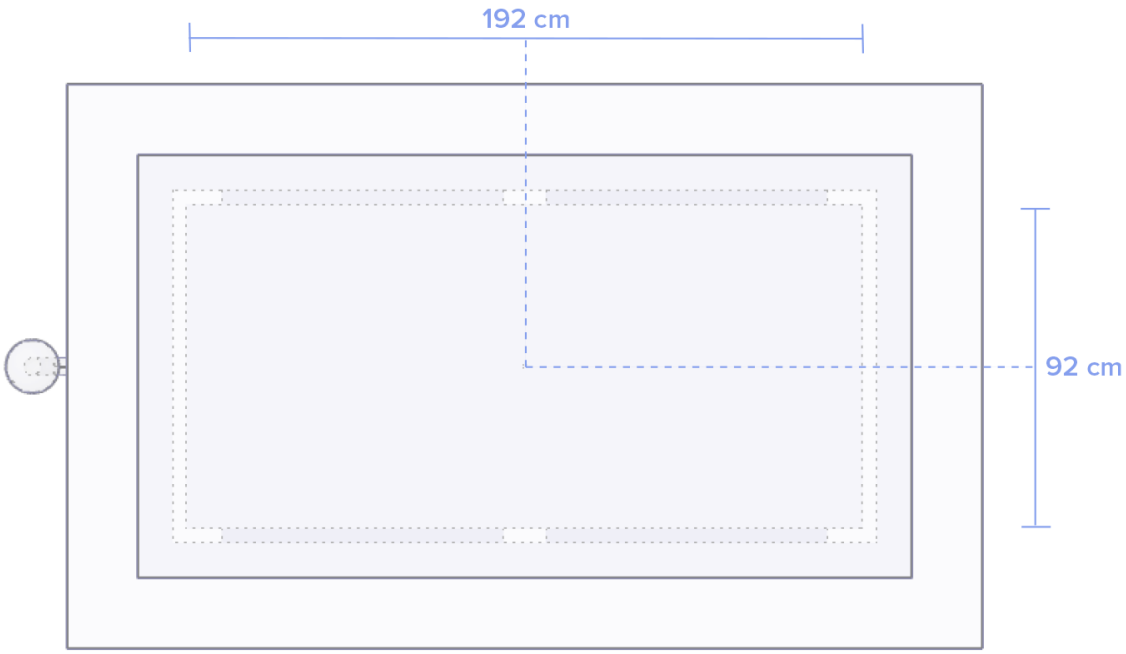

Figure A.1: Scenario 2 cabin top view.

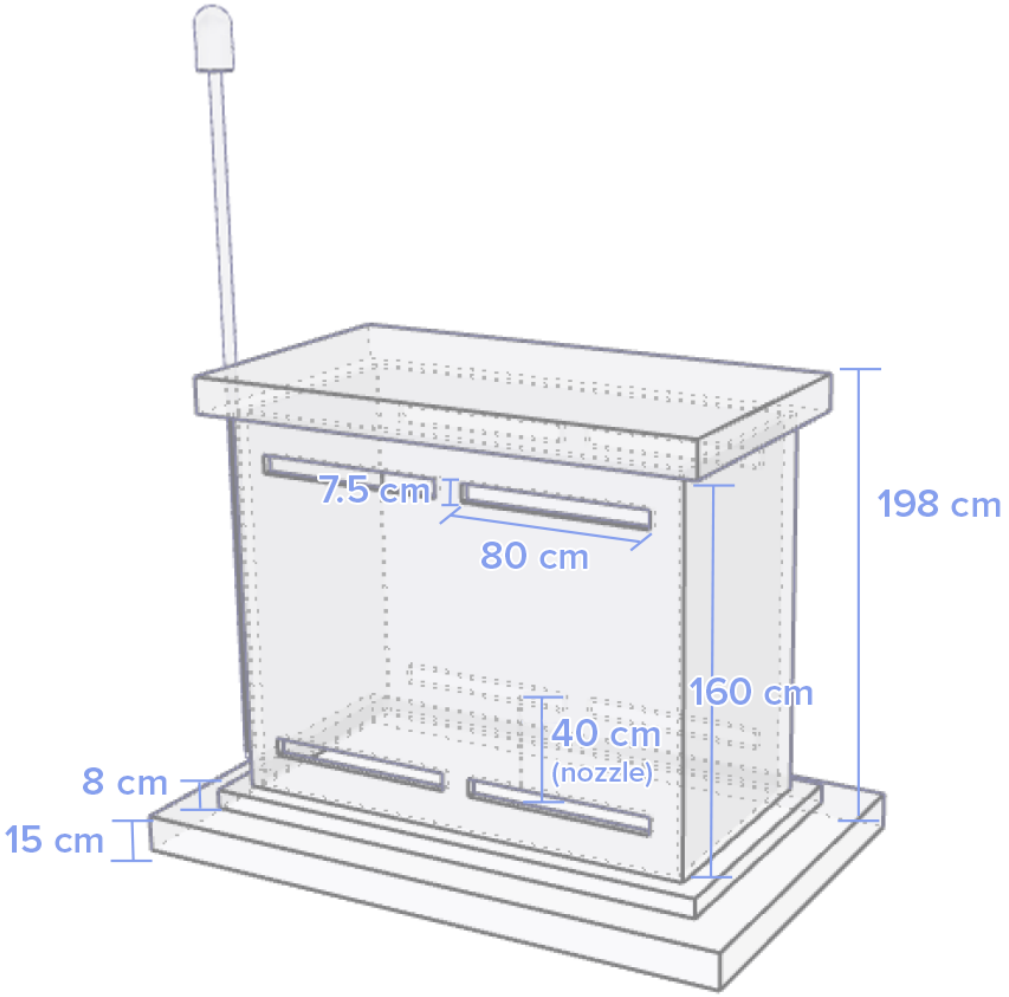

Figure A.2: Scenario 2 cabin perspective view.

A.2. Scenario 3

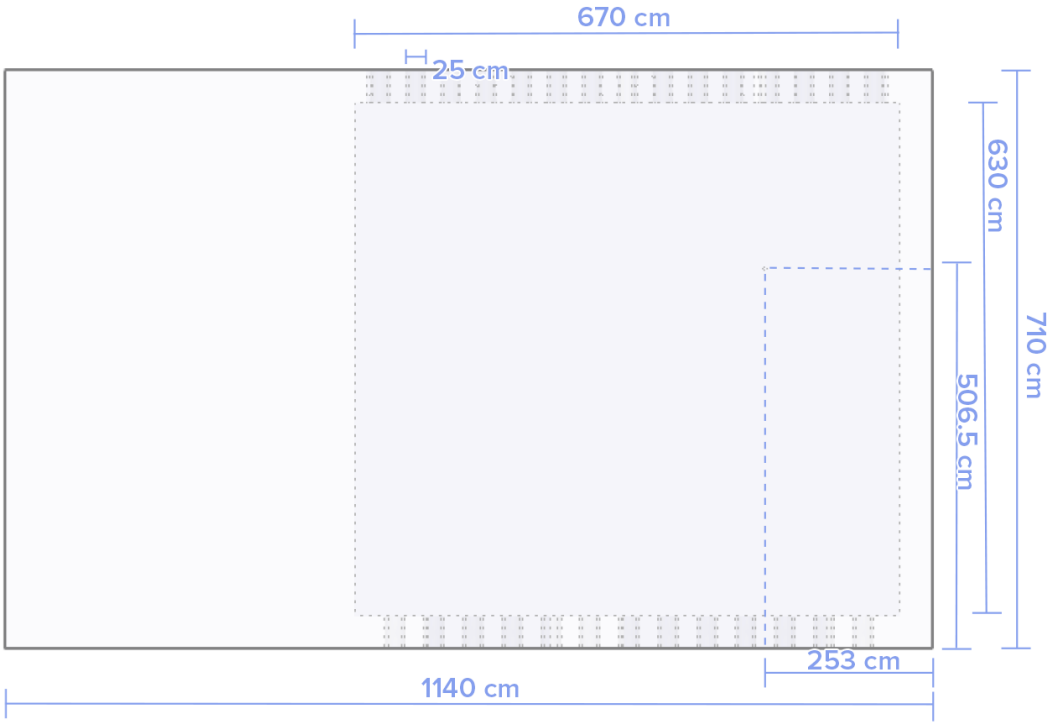

Figure A.3: Scenario 3 top view.

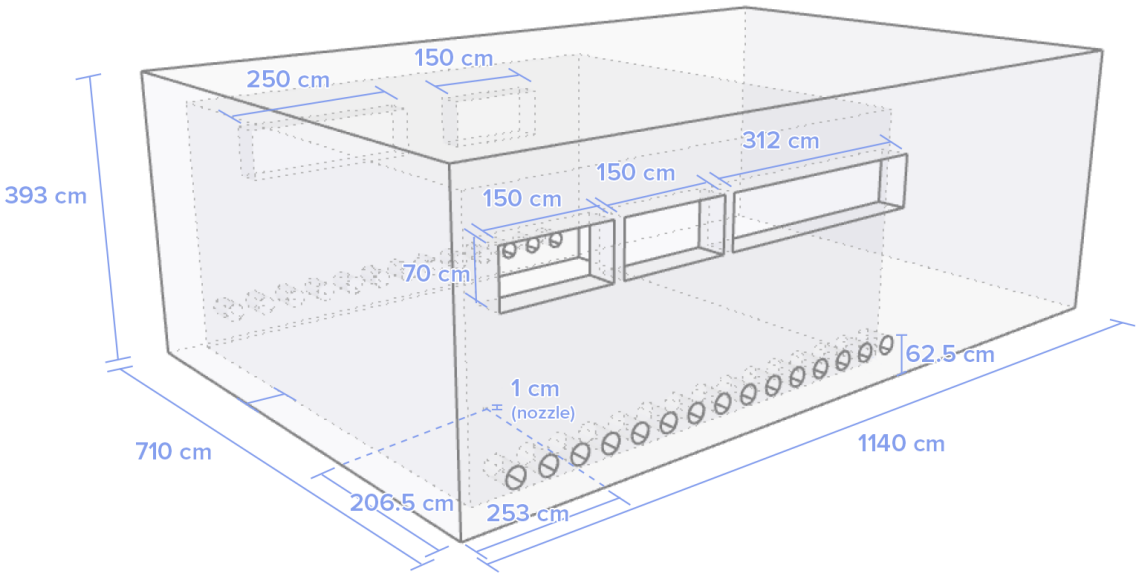

Figure A.4: Scenario 3 perspective view.

A.3. Scenario 4

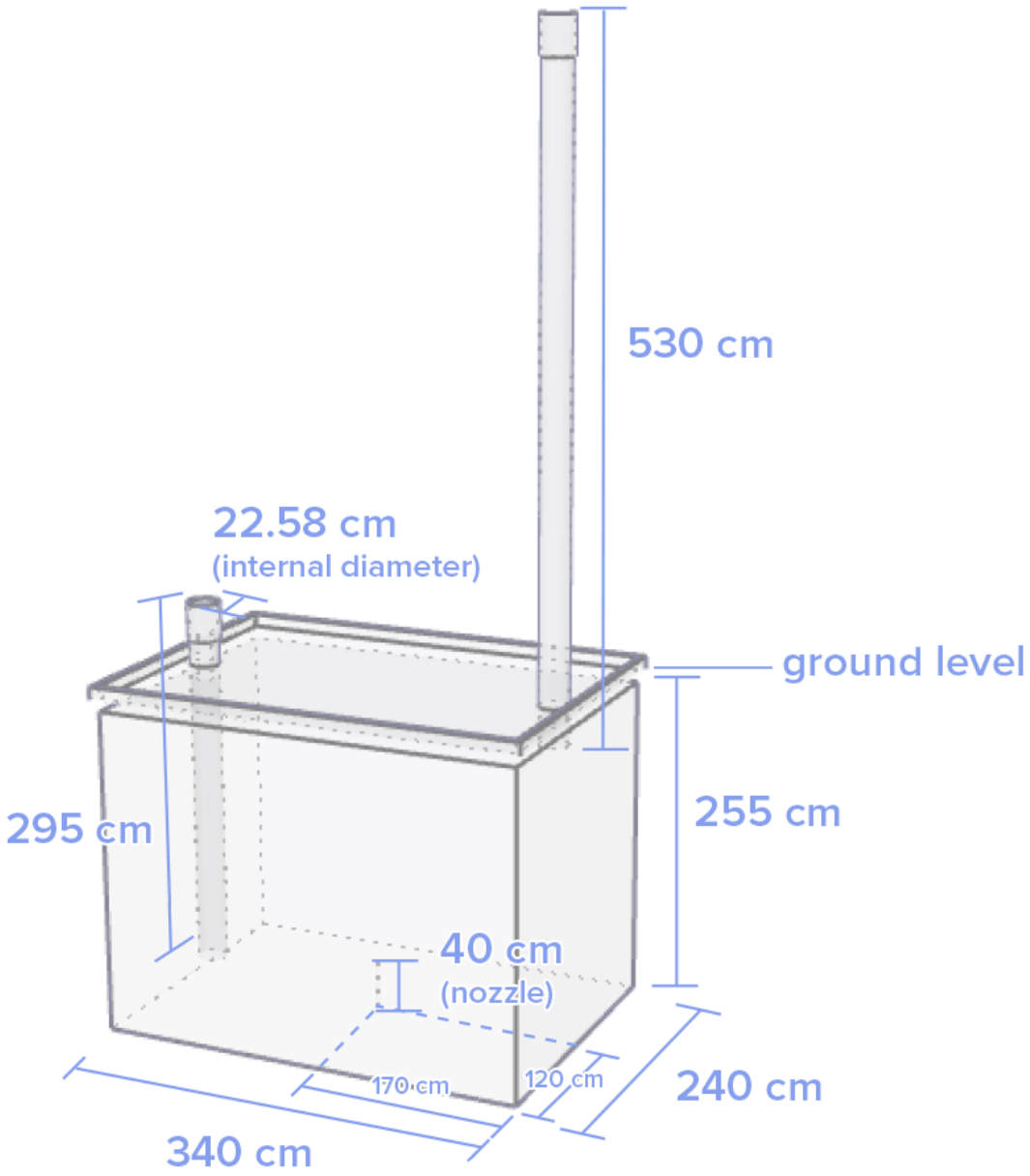

Figure A.5: Scenario 4 perspective view.

A| Appendix A:
3D model dimensioning of scenarios

List of Figures

List of Tables

List of Symbols

Variable	Description	SI unit
$\boldsymbol{u}$	solid displacement	m
$\boldsymbol{u}_f$	fluid displacement	m
C_{LFL}	LFL concentration	vol%
C_{UFL}	LFL concentration	vol%
D	diameter	m
ρ_{air}	air density	kg/m3
ρ_{gas}	gas density	kg/m3
S_c	Schmidt Number	-
v	velocity	m/s
V_{eq}	equivalent diameter velocity	m/s
M_w	molecular weight	g/mol
ρ_{eq}	equivalent density	kg/m3
T_{eq}	equivalent temperature	K
P_{eq}	equivalent pressure	Pa
R	gas constant	J/mol/K
C_p	specific heat capacity	J/kg/K

Acknowledgements

I have been able to successfully complete this thesis work and, in general, my academic journey, thanks in large part to the support of the people closest to me. In particular, I would like to express my heartfelt gratitude to my family, my dearest friends, my university peers, and my colleagues who assisted me during my internship at the company.

Thank you all.